Palaeogeography, Palaeoclimatology, Palaeoecology 592 (2022) 110903

Contents lists available at ScienceDirect

Palaeogeography, Palaeoclimatology, Palaeoecology

journal homepage: www.elsevier.com/locate/palaeo

Hypersalinity accompanies tectonic restriction in the eastern Mediterranean prior to the Messinian Salinity Crisis

George Kontakiotis [a,*,1], Geanina A. Butiseacă [b,c,**,1], Assimina Antonarakou [a], Konstantina Agiadi [d], Stergios D. Zarkogiannis [e], Emilija Krsnik [b,c], Evangelia Besiou [a], Willem Jan Zachariasse [f], Lucas Lourens [f], Danae Thivaiou [a], Efterpi Koskeridou [a], Pierre Moissette [a,g], Andreas Mulch [b,c], Vasileios Karakitsios [a], Iuliana Vasiliev [b]

[a] Faculty of Geology and Geoenvironment, School of Earth Sciences, Department of Historical Geology-Paleontology, National and Kapodistrian University of Athens, Panepistimiopolis, Zografou, 15784, Athens, Greece
[b] Senckenberg Biodiversity and Climate Research Centre (SBiK-F), Senckenberganlage 25, D-60325 Frankfurt am Main, Germany
[c] Institute of Geosciences, Goethe University Frankfurt, Altenhöferallee 1, 60438 Frankfurt am Main, Germany
[d] Department of Palaeontology, Faculty of Earth Sciences, Geography and Astronomy, University of Vienna, Althanstrasse 14, Geozentrum (UZA II), 1090 Vienna, Austria
[e] Department of Earth Sciences, University of Oxford, Oxford OX1 3AN, UK
[f] Faculty of Geosciences, Department of Earth Sciences, Utrecht University, Budapestlaan 4, 3584 CD Utrecht, the Netherlands
[g] Muséum National d'Histoire Naturelle, Département Origines et Evolution, UMR7207 CR2P, 8 rue Buffon, 75005 Paris, France

ARTICLE INFO

Editor: Howard Falcon-Lang

Keywords:
Sea surface temperature
Sea surface salinity
Step-wise restriction
Messinian Salinity Crisis
Tectonics-climate interplay
Environmental stress

ABSTRACT

This study describes the hydroclimate evolution of the eastern Mediterranean Basin during the early Messinian (7.2 to 6.5 Ma) time-interval based on analysis of a succession at Agios Myron (Crete, Greece), prior to the onset of the Messinian Salinity Crisis (5.96–5.33 Ma). Specifically, we report sea surface temperature and salinity reconstructions based on a combined analysis of biomarkers and oxygen isotopes of planktonic foraminifera. Data reveal that a negative water budget and strong hydrologic and climate variability characterized the eastern Mediterranean Basin at this time, and we identify three distinct phases. In Phase 1 (7.2–6.9 Ma), a shift to more positive oxygen isotope values in planktonic foraminifera at ~7.2 Ma is attributed to progressive gateway restriction of Mediterranean–Atlantic corridors and subsequent cooling until 6.9 Ma. In Phase 2 (6.9–6.7 Ma), distinct warm and hypersaline events (at 6.9–6.82 and 6.72 Ma) resulted in stressed marine microfauna during periods of strong evaporation. An important step-change in the Mediterranean restriction at 6.72 Ma may have resulted from shallowing of the Mediterranean gateways and reduced Mediterranean marine outflow. During Phase 3 (6.7–6.5 Ma) this gateway shallowing reduced the oceanic input into the Mediterranean Basin causing significant hydrological changes, reflected in a wide range of temperature and salinity fluctuations accompanied by enhanced water-column stratification. The data presented here counterbalance the general lack of quantitative temperature and especially salinity estimates available for the Mediterranean Messinian, time interval where we still highly rely on modelling for such evaluations. This study highlights the severity of preconditioning stages leading to the Messinian Salinity Crisis in the Mediterranean and sets values for extreme salinity conditions that could still host marine life.

1. Introduction

In the Mediterranean Basin, the latest Miocene stands out as a period of extreme environmental conditions, culminating with the Messinian Salinity Crisis (MSC) at 5.97–5.33 Ma (Krijgsman et al., 1999a; Manzi et al., 2013; Roveri et al., 2014). Severe restriction of connection to the open ocean characterized the MSC, ultimately leading to dramatic lowering of Mediterranean sea-level (e.g., Hsü et al., 1973; Capella et al.,

* Corresponding author.
** Corresponding author at: Senckenberg Biodiversity and Climate Research Centre (SBiK-F), Senckenberganlage 25, D-60325 Frankfurt am Main, Germany.
E-mail addresses: gkontak@geol.uoa.gr (G. Kontakiotis), butiseacageanina@gmail.com (G.A. Butiseacă).
[1] Equal correspondence between the two first authors with equal contribution.

https://doi.org/10.1016/j.palaeo.2022.110903
Received 27 January 2022; Received in revised form 28 February 2022; Accepted 28 February 2022
Available online 5 March 2022

2019; Flecker et al., 2015; Madof et al., 2019). During the Messinian stage (7.25–5.33 Ma), tectonic processes in the Rifian and Betic gateways (Fig. 1) together with glacio-eustatic sea-level oscillations led to isolation of the Mediterranean Basin from the Atlantic Ocean (e.g., Capella et al., 2019; Krijgsman et al., 2018), initially triggering the cyclic deposition of bio-siliceous deposits of the Tripoli Formation consisting of alternations of marls, limestones, diatomites and sapropels (Blanc-Valleron et al., 2002) and finally to the widespread deposition of massive evaporites (Hsü, 1972). These Messinian Mediterranean deposits have sparked intense interest in the sedimentology, cyclostratigraphy, paleontology and geochemistry of such prolonged restriction events (e.g., Hilgen and Krijgsman, 1999; Karakitsios et al., 2017a, 2017b; Moissette et al., 2018; Roveri et al., 2014; Sabino et al., 2020, 2021; Sierro et al., 2003; Vasiliev et al., 2017, 2019). Interestingly, the detailed sequence of Messinian events and their relationship to paleoceanography and global climate (i.e., sea level changes, hydrological budget, water-column characteristics and ecosystem response) remain poorly understood, mainly due to the scarcity of continuous, high-resolution climate and paleoceanographic archives (e.g., Tzanova et al., 2015; Zachariasse et al., 2021; Zachariasse and Lourens, 2021). Most available records cover long-term trends, but do not capture short-term climate events and relationships required to assess high-frequency changes in sea surface temperature (SST) and sea surface salinity (SSS), parameters acting as main drivers of thermohaline circulation. Moreover, the particularity of such surface and/or bottom water changes from the eastern Mediterranean is that any pre-MSC paleoceanographic and paleoclimatic signal will be recorded in an amplified fashion due to the greater distance from the Gibraltar (Atlantic connection). Overall, this heightened sensitivity to the effects of climate variability, in terms of restrictions, underlines the prominent role of such marginal eastern Mediterranean sub-basins in the understanding of the MSC and global climate evolution during that period.

Here we present SST and SSS changes recorded in the Agios Myron section (central Crete, Greece), a sedimentary succession hosting early Messinian (~7.2–6.5 Ma) rhythmic sapropel-marl couplets. The cyclic sedimentary pattern is also recorded in oxygen stable isotope ratios ($\delta^{18}O$) of the climate-sensitive surface-dwelling planktonic foraminiferal species *Globigerinoides obliquus* and both Tetra Ether Index (TEX_{86}) and alkenone unsaturation ratio ($U^{K}_{37}{}'$) biomarker-based paleotemperature proxies. The combined TEX_{86}- and/or $U^{K}_{37}{}'$-SST reconstructions as well as the *G. obliquus* $\delta^{18}O$ record further allow to evaluate changes in the early Messinian hydrology as recorded in the oxygen isotope composition of Mediterranean seawater ($\delta^{18}O_{SW}$). We discuss these combined SSS and SST records in the context of marine productivity, basin stratification and river runoff, as these are fundamental for the interpretation of the geochemical signals and the paleoceanographic evolution of the eastern Mediterranean before the MSC onset. Finally, we compare all the above paleoenvironmental data with previously published coeval Mediterranean records (Kontakiotis et al., 2019; Mayser et al., 2017; Tzanova et al., 2015; Vasiliev et al., 2019) to highlight the processes driving and regulating the hydrographic changes in the eastern Mediterranean Basin and the relation to its far end location relative to the Atlantic gateway.

2. Regional setting

2.1. Geological setting

The eastern Mediterranean Basin (Fig. 1) is a relic of the Neotethys Ocean in the Tethys domain, shaped by the collision and continued convergence of the African, Arabian and Eurasian plates (e.g., Robertson et al., 2012). The island of Crete, situated in the central part of the basin (Fig. 1), is part of the forearc accretionary zone and exhibits a horst structure that consists of a metamorphic nappe pile with sediments from various paleogeographical zones (e.g., van Hinsbergen and Meulenkamp, 2006). The uplift and exhumation of the nappe pile were accompanied by the structural fragmentation of the pre-Miocene basement to several blocks, which created new accommodation space by displacement during the Lower to Middle Miocene. The Heraklion Basin is one of the largest Neogene sedimentary basins of Crete, developed in the hanging wall of the Cretan detachment and filled with fluvial to deep marine Tortonian to Pliocene sedimentary rocks (e.g., van Hinsbergen and Meulenkamp, 2006; Zachariasse et al., 2011), but the present-day high topography of the surrounding mountains was largely shaped during the Pleistocene (e.g., Zachariasse et al., 2021). The northern block of the Heraklion Basin, hosting the Agios Myron section, emerged after 9.6 Ma and remained emerged until the latest Tortonian (~7.4 Ma) (Zachariasse et al., 2011, 2021). Subsequently, intermittent subsidence

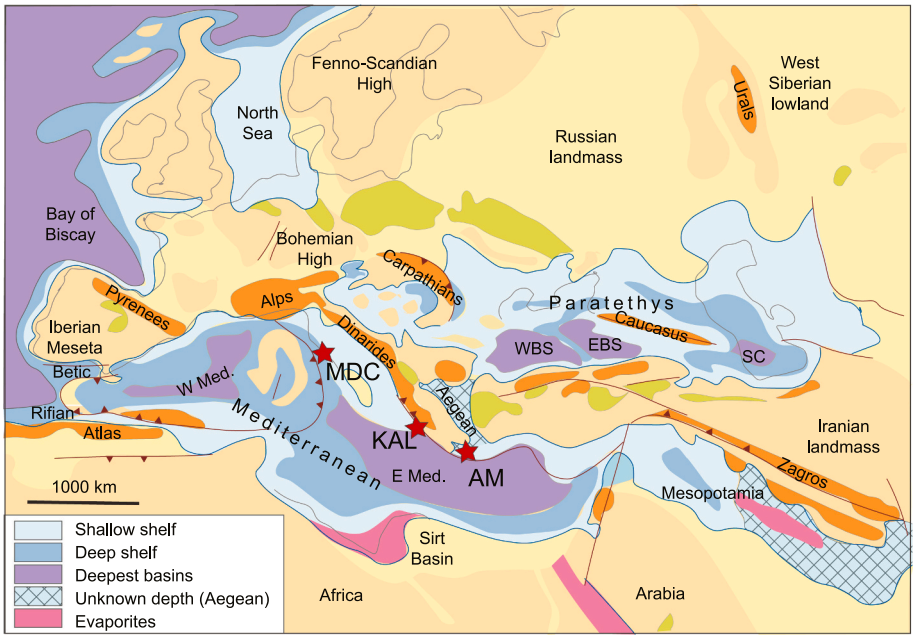

Fig. 1. Paleogeography map for the Mediterranean-Paratethys domain during late Miocene (Ilyina et al., 2004). Note the paleolatitudinal location and their approximate position within the late Miocene Mediterranean basin for Agios Myron (AM), Kalamaki (KAL) and Monte dei Corvi (MDC) sections.

to upper bathyal depths in the early Messinian is manifested by the Agios Myron Formation (Zachariasse et al., 2021 and references therein).

2.2. The Agios Myron section: lithology and chronometric scale

The Agios Myron section, in central Crete (N 35°23′35.90", E 25°12'67.91"), is the result of continuous hemipelagic sedimentation during the early Messinian (7.2 to 6.5 Ma). The section is ~25 m thick and consists of blueish-grey silty marls without clear sedimentary cyclicity in the basal seven meters, followed by a rhythmic alternation of blueish-grey homogeneous and brownish laminated marls (referred to here as sapropels) with three distinct ash layers (numbered 1 to 3) in the overlying 18 m (Fig. 2). The Agios Myron region began to subside in the latest Tortonian and, based on the sudden appearance of sapropels, passed the upper depth limit for sapropel formation at 7.05 Ma (Zachariasse et al., 2021). The cyclically bedded sequence records 24 sedimentary cycles characterized by couplets of homogenous marls and sapropels, with an average sedimentation rate of 3.53 cm/kyr. The nature of the sedimentary cycles closely resembles other astronomically calibrated early Messinian Mediterranean sequences, with up to 32 documented precession cycles present between 7.2 and 6.5 Ma (Hilgen et al., 1995, 2000).

The robust stratigraphic time frame of the Agios Myron section is supported by the identification of planktonic foraminiferal bioevents, tephra layers and the overall correlation of bipartite sedimentary cycles with those of the nearby orbitally-tuned Metochia section, the reference section for the Messinian in the eastern Mediterranean (Zachariasse et al., 2021). In particular, biostratigraphic events and tephra layers were used as reference points when correlating the identified cycles to the overall reference frame given in Hilgen et al. (1995) and Hilgen and Krijgsman (1999). The first and the last occurrence (FO and LO) of *Globorotalia nicolae*, astronomically tuned to 6.83 and 6.72 Ma in the Mediterranean Basin (Hilgen et al., 1995; Hilgen and Krijgsman, 1999; Lourens et al., 2004), were identified in samples AM 13C and AM 08, respectively. The Cretan ash layers 1 to 3 with the astronomical ages of 6.941, 6.887 and 6.771 Ma (Hilgen et al., 1997; Kuiper et al., 2004) are stratigraphically located below samples AM 18, AM 16 and AM 10, respectively. The resulting age model is based on the two astronomically-calibrated planktonic foraminiferal bioevents, the three ash layers and supplemented by the additional dating of the mid points of the sapropel layers, assuming constant sedimentation rates between them and established by linear interpolation between all control points (Fig. 2). The age control for the lowermost four samples is less well defined in the absence of biostratigraphic events and visible lithological cycles. However, these four oldest samples all belong to the earliest Messinian based on the continuous presence of *Globorotalia miotumida*. They are, therefore, younger than 7.25 Ma and older than the first well-dated sample at 7.05 Ma.

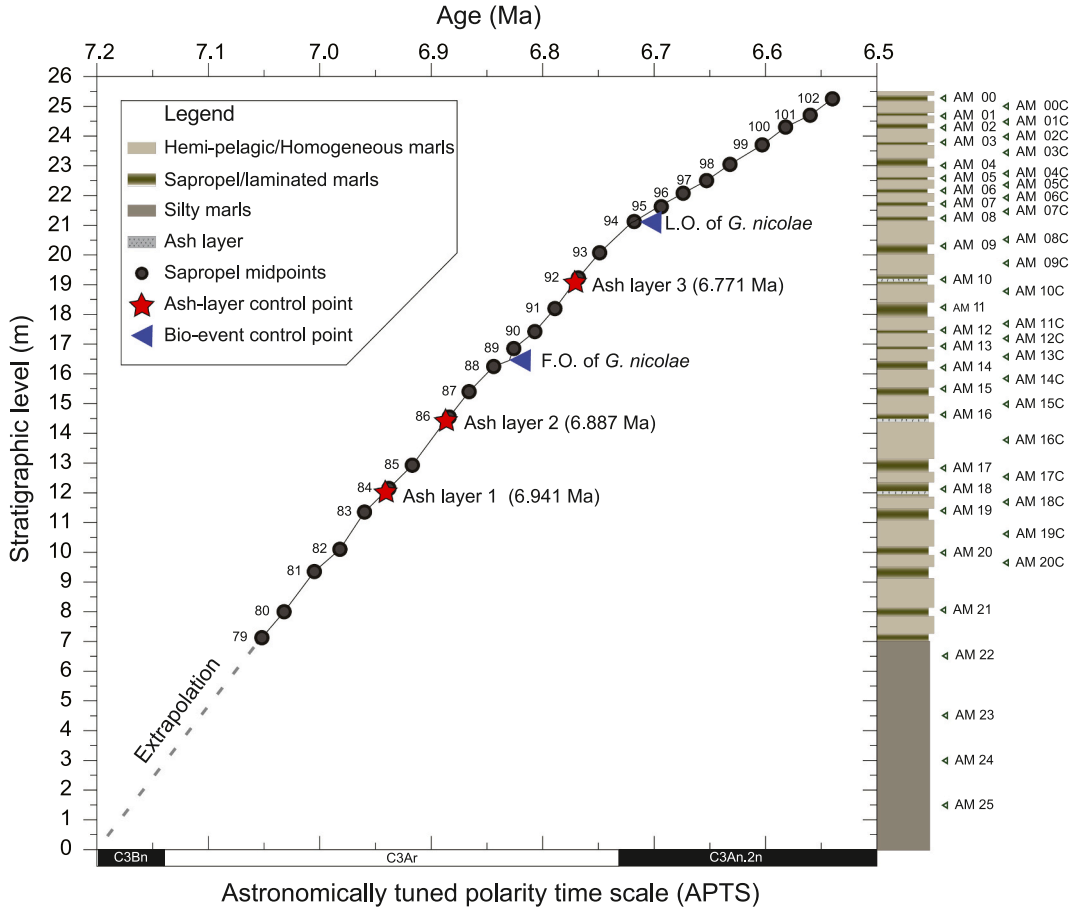

Fig. 2. Age model of the study section created by linear interpolation between all control points (two planktonic foraminiferal bioevents symbolized with blue arrowheads, three tephra layers symbolized with red stars, and 24 astronomically dated sapropel midpoints for identified sedimentary cycles symbolized with black dots), as defined by the recent bio-cyclostratigraphic work of Zachariasse et al. (2021). The numbers next to black dots correspond to Metochia sedimentary cycles for the time-equivalent interval. At the lower part of the figure the polarity pattern of the astronomically dated polarity time scale (APTS; Lourens et al., 2004) is presented. In the right-hand side, the schematic lithological column of Agios Myron is shown with the location of the analyzed samples. (For interpretation of the references to colour in this figure legend, the reader is referred to the web version of this article.)

3. Material and methods

3.1. Lipid extraction, fraction separation and biomarker analysis

Forty-seven sedimentary rock samples were collected with an average spacing of 160 cm (34 kyr) for the basal silty marls and 40 cm (12 kyr) for the cyclically bedded marls and subjected to geochemical (biomarker and isotope) analyses. The samples (30–60 g weight) were dried and powdered using a pre-cleaned agate mortar and pestle. Lipids were extracted using a Soxhlet apparatus with a mixture of dichloromethane (DCM) and methanol (MeOH) (7.5:1; *v:v*) and pre-extracted cellulose filters. All extracts were evaporated to near dryness under N_2 flow with a TurboVap LV obtaining the total lipid extracts (TLE). Subsequently, elemental sulphur was removed using Cu shreds. The Cu was activated using 10% HCl, then rinsed with demineralized water until reaching neutral pH and further cleaned using MeOH and DCM. The TLE vials containing the activated Cu and magnetic rods were placed on a rotary table for ~16 h. The samples were filtered over a Na_2SO_4 column and dried subsequently. Desulphurization was repeated until no reaction with Cu was observed. A fraction of the TLE was archived. The remaining TLE were then separated into fractions by Al_2O_3 column chromatography based on mixtures of solvents of increasing polarity. The apolar fraction was eluted using a mixture of *n*-hexane and DCM (9:1, *v:v*), the ketone fraction using DCM, and the polar fraction using a mixture of DCM/MeOH (1:1, *v:v*). The ketone fraction containing alkenones was purified using an $AgNO_3$ column and ethyl acetate. Alkenones were identified using Gas Chromatography-Mass Spectrometry (GC–MS) at the Senckenberg Biodiversity and Climate Research Centre (SBiK-F) in Frankfurt am Main. The fractions (dissolved in *n*-hexane) were injected on-column at 70 °C (CP-Sil 5CB fused silica column (30 m × 0.32 mm i.d; film thickness 0.12 μm). The oven was set at constant pressure (100 kPa) and then programmed to increase to 130 °C at 20 °C min^{-1}, and to 320 °C at 5 °C min^{-1} at which it was held isothermal for 10 min. The polar fraction containing glycerol dialkyl glycerol tetraethers (GDGTs) was dried under N_2 then dissolved in a 1 ml mixture of *n*-hexane (*n*-hex)/isopropanol (IPA) (99:1, *v:v*) and dispersed using an ultrasonic bath (30 s), then filtered over a 0.45 mm PTFE filter using a 1 ml syringe. The filtered polar fraction containing GDGTs was analyzed at SBiK-F using an HPLC Shimadzu, UFLC performance (analytical column Alltech Prevail© Cyano 3 mm, 150–2.1 mm; eluents *n*-hex (A) and IPA (B) coupled with an ABSciex 3200 QTrap chemical ionization mass spectrometer (HPLC/APCIeMS). The injection volume was 5 ml. GDGTs were eluted isocratically from 0 to 5 min with 1% (B); then with a gradient to 1.8% (B) from 5 to 32.5 min, ramped to 30% (B) to min 33.5, held 10 min, back to 1% (B) in 1 min. Detection was achieved through single ion monitoring (scanned masses: 1018, 1020, 1022, 1032, 1034, 1036, 1046, 1048, 1050, 1292, 1296, 1298, 1300, 1302). Quantification of GDGTs was performed using the Analyst software.

3.2. Temperature proxies

Temperature estimates were obtained using both the TEX_{86} (Kim et al., 2010; Schouten et al., 2002, 2013) and $U^{K}_{37}{}'$ (Brassell et al., 1986; Prahl and Wakeham, 1987) proxies. The former is based on the ratio of isoprenoidal (iso)GDGTs mainly produced by the *Archaea* group (Schouten et al., 2013), whereas the latter is based on the unsaturation of long-chain alkenones produced by haptophyte algae (Volkman et al., 1995). Both proxies exhibit a strong relationship with SST (e.g., Conte et al., 2006; Kim et al., 2008, 2010; Müller et al., 1998; Schouten et al., 2002). Using both TEX_{86} and $U^{K}_{37}{}'$ was necessary due to the absence of alkenones in 23 out of the total of 47 analyzed samples. Parallel TEX_{86} and $U^{K}_{37}{}'$ based SST are, therefore, presented for only 24 levels.

3.2.1. Sea surface temperature estimates based on TEX^{H}_{86}

TEX_{86} values were calculated as follows (Schouten et al., 2002):

$$TEX86 = \frac{[GDGT-2]+[GDGT-3]+[Cren']}{[GDGT-1]+[GDGT-2]+[GDGT-3]+[Cren']}$$

where *GDGT-1*, *GDGT-2, GDGT-3* and *Cren'* are isoprenoid GDGTs with the structures presented in Supplementary Fig. 1. TEX_{86} values were converted into SST using the calibration and recommendation of Kim et al. (2010) to apply the $TEX_{86}{}^{H} > 15$ °C for regions outside the polar and subpolar latitudes as follows:

$$TEX^{H}_{86} = log\,(TEX_{86}) \text{ and the SST based on } TEX_{86}{}^{H}\ \left(TEX^{H}_{86} - SST\right)$$

$$TEX^{H}_{86} - SST = 68.4 \times (\text{GDGT index} - 2) + 38.6,\ \left(r^2 = 0.87, p < 0.0001\right).$$

Where

$$GDGT\ index - 2 = log\frac{[GDGT-2]+[GDGT-3]+[Cren']}{[GDGT-1]+[GDGT-2]+[GDGT-3]+[Cren']}$$

SST calculations based on $TEX_{86}{}^{H}$ has a calibration residual standard (1σ) error of ±2.5 °C and is based upon 255 core-top sediments.

3.2.2. Sea surface temperature estimates based on $U^{K}_{37}{}'$

SST estimates were based on the degree of unsaturation of C_{37} alkenones ($U^{K}_{37}{}'$), which is primarily a function of temperature (Müller et al., 1998), by monitoring the ratio between the di- and tri-unsaturated alkenones:

$$UK37' = \frac{C37:2}{C37:2 + C37:3}$$

We used the transfer function $U^{K}_{37}{}' = 0.033\ T\ [°C] + 0.044$ (± 1 °C), based on a global core-top calibration (Müller et al., 1998).

3.3. Stable oxygen isotope ratios ($\delta^{18}O$) of planktonic foraminifera

Forty-seven sediment samples were collected and processed following standard geochemical procedures. In short, the sedimentary rock samples were oven-dried at 50 °C overnight, weighed, and disaggregated in ultraclean water for six hours on a shaker table. To collect the coarse fraction, samples were wet-sieved using a 63 μm mesh. Residues were sieved into sub-fractions for isotopic analyses. For $\delta^{18}O$ measurements, five *Globigerinoides obliquus* specimens were handpicked, at every level, from the 250–300 μm sieve fraction. This number of individuals was necessary to supply sufficient $CaCO_3$ (~100 μg) and to limit the effect of individual variation on the $\delta^{18}O$ values, while the adopted size fraction was used to minimize intraspecific ontogenetic and growth rate effects on shell geochemistry (Elderfield et al., 2002). The choice of the shallow-dwelling species *G. obliquus* for $\delta^{18}O$ was made following earlier works of Seidenkrantz et al. (2000) and Kontakiotis et al. (2016, 2019) studying changes in the Mediterranean surface waters during the Neogene. Once picked, specimens were sonicated in MeOH for about 10 s to remove clay particles adhering to the *G. obliquus* tests and further rinsed five times in ultraclean water. The observation of shell microstructure of randomly selected specimens using a Jeol JSM 6360 Scanning Electron Microscopy (SEM) confirmed the relatively good preservation regime, based on their 'frosty' appearance (Antonarakou et al., 2019). All picking, cleaning, and diagenesis screening were performed at the Department of Historical Geology-Paleontology in Athens. Isotopic analyses were performed using a *Thermo 253, Thermo GasBench II* coupled to a *Thermo 253* isotope ratio mass spectrometer in continuous flow mode, thermostated sample tray and a *GC PAL* autosampler at the Goethe Universität – Senckenberg BiK-F Joint Stable Isotope Facility. During the project, analytical precision was 0.07‰ for $\delta^{18}O$. Replicates of 10% of the data reveal that reproducibility and natural sample variability are better than 0.1‰. Results are reported against Vienna Pee Dee Belemnite (VPDB) using the standard δ notation expressed in per mil (‰).

3.4. Estimates of sea surface salinity

Foraminiferal $\delta^{18}O$ records are a function of temperature and the ambient oxygen isotopic composition of seawater ($\delta^{18}O_{SW}$) in which the shell precipitated, which in turn depends on global ice volume and ocean salinity. If the temperature (T) component is accounted for, foraminiferal calcite $\delta^{18}O$ can be used to estimate past changes in salinity, because $\delta^{18}O_{SW}$ co-varies linearly with SSS (e.g., LeGrande and Schmidt, 2006), as both increase with evaporation and decrease through admixture of low-$\delta^{18}O$ freshwater. Based on this concept and in accordance with earlier studies (e.g., Antonarakou et al., 2015; Kontakiotis et al., 2019; Vasiliev et al., 2019), we used a multiproxy geochemical approach to estimate regional past SSS variability. To isolate the $\delta^{18}O_{SW}$ from the measured foraminiferal $\delta^{18}O_C$ values, the temperature component was removed using the *Orbulina universa* low-light paleotemperature equation of Bemis et al. (1998):

$$T = 16.5\text{–}4.80^{*}\left(\delta^{18}O_C - \left(\delta^{18}O_{SW} - 0.27‰\right)\right) (\pm 0.7^{\circ}C)$$

Although the Bemis et al. (1998) equation has been calibrated within the range of 15–25 °C, its extrapolation to even higher temperatures (up to 30 °C) provides good agreement with field data in warmer environments (e.g., Sargasso Sea, Indian Ocean; Bouvier-Soumagnac and Duplessy, 1985; Williams et al., 1981), overall reflecting the entire temperature range observed into the Mediterranean during the Messinian. Moreover, the used equation has been considered as the most accurate equation for estimating paleo-SST (including the late Miocene) for symbiotic planktonic foraminifera in subtropical settings (Williams et al., 2005).

Removing temperature from the $\delta^{18}O$ record using the above equation yields the salinity proxy. To correct for the continental ice volume effect, we used the late Miocene record of eustatic sea level changes as modeled by Miller et al. (2011). Briefly, we linearly interpolated the Miller et al. (2011) record at the study time period, generated a record of global $\delta^{18}O_{SW}$ change (resulting from the melting of continental ice sheets) over the Messinian by converting the sea-level data into mean ocean $\delta^{18}O$ changes and applying a 0.008‰ increase per meter of sea-level lowering (Siddall et al., 2003), and then subtracted this component from the $\delta^{18}O_{SW}$ profile to obtain the regional ice volume free $\delta^{18}O_{SW}$ ($\delta^{18}O_{IVF\text{-}SW}$) residual. The calculated $\delta^{18}O_{IVF\text{-}SW}$ values are due to changes in regional hydrography and therefore considered to approximate local variations in SSS. The $\delta^{18}O_{IVF\text{-}SW}$ record has merely an illustrative character and therefore is used to investigate the potential salinity effect on our results. To convert the $\delta^{18}O$ signal to absolute SSS values we used the modern $\delta^{18}O_{sw}$–Salinity relationship for the Mediterranean Sea $\delta^{18}O = 0.25^{*}S - 8.2$, exclusively considering the dataset which reflects surface waters with salinities higher than 36.2 (Pierre, 1999).

4. Results

4.1. Sea surface TEX^{H}_{86} and $U^{K}_{37}{}'$ based temperatures

The TEX^{H}_{86}-SST estimates range between 20.7 and 30.0 °C (average

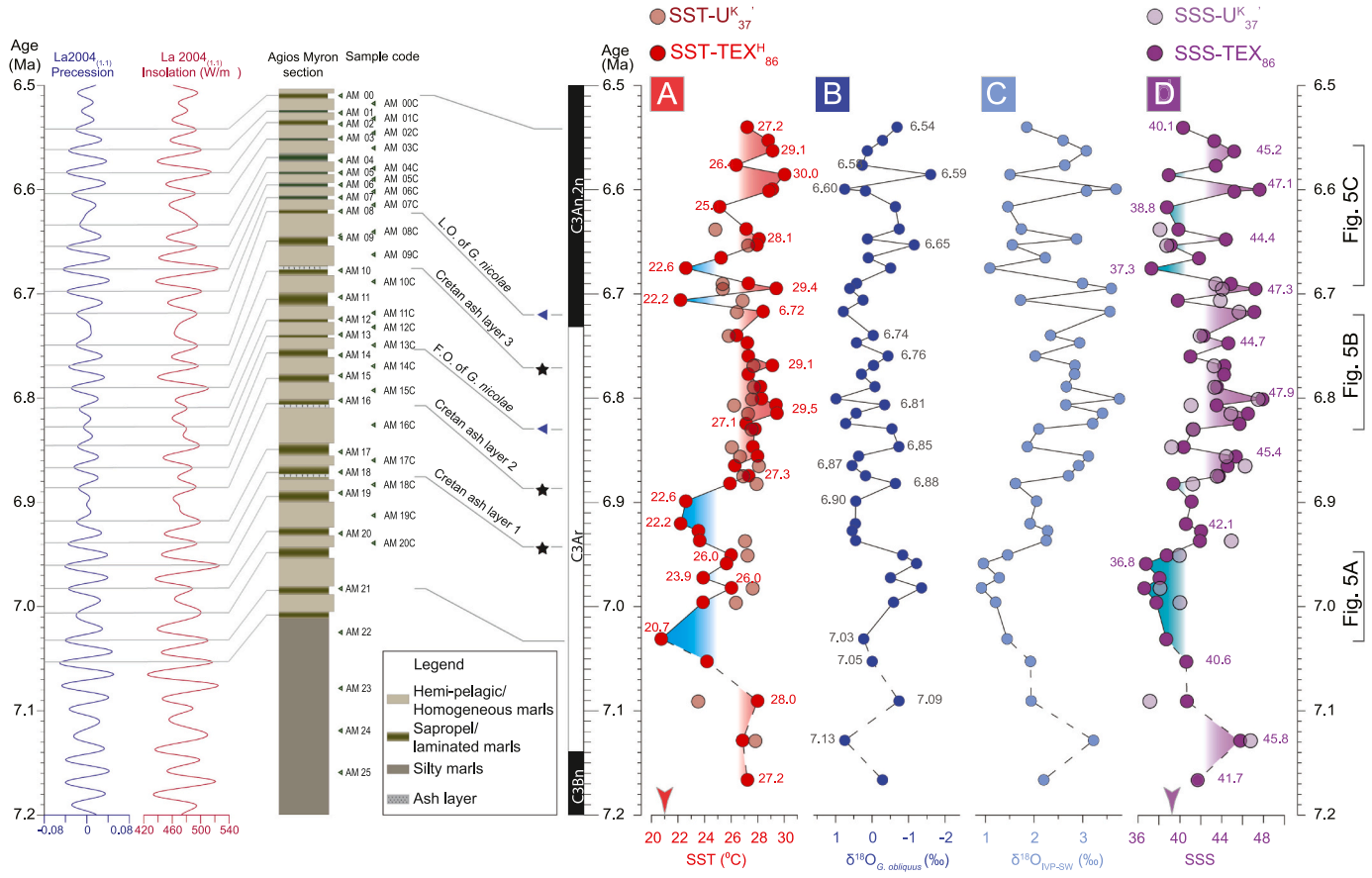

Fig. 3. Agios Myron A) Sea surface temperature calculated based on TEX^{H}_{86} (SST-TEX^{H}_{86}) and on $U^{K}_{37}{}'$ (SST-$U^{K}_{37}{}'$); B) $\delta^{18}O$ measured on *Globigerinoides obliquus* ($\delta^{18}O_{G\text{-}obliquus}$); C) ice volume-free $\delta^{18}O$ surface sea water (IVF-$\delta^{18}O_{SW}$); D) sea surface salinities (SSS) based on SST-TEX^{H}_{86} and SST-$U^{K}_{37}{}'$. On the left side is the astronomical precession and insolation summer curve of Laskar et al. (2004), the lithological column, samples names and position, bioevents and ash layers used for calibration to the APTS (Lourens et al., 2004). For clarity, the red numbers next to SST data are obtained temperature estimates based on TEX^{H}_{86}, the grey numbers next to $\delta^{18}O_{G.\ obliquus}$ points indicate ages in Ma, while the purple numbers next to SSS indicate calculated salinity based on SST-TEX^{H}_{86}. The arrows indicate the present-day values for SST and SSS. (For interpretation of the references to colour in this figure legend, the reader is referred to the web version of this article.)

26.6 °C), indicating almost 10 °C variation in the Agios Myron section (Fig. 3A; Supplementary table). Three intervals show TEX^{H}_{86}-SST values lower than 23 °C (at ~7.03, 6.91 and 6.68 Ma). The remainder of the record shows consistently higher SSTs. When analyzing the SST trends, the TEX^{H}_{86}-SSTs start with values averaging around 27 °C, from the base of the sampled section (7.17 Ma–7.09 Ma). Afterwards, the first cooling step (20.7 °C) takes place until ~7.03 Ma, followed by a warming to 26 °C between 7.00 and 6.95 Ma. A marked cooling (to 22 °C) occurs around 6.91 Ma, after which the SSTs increase again to steady values of ~27 °C, with a low variability (6.88–6.69 Ma). In this 190 kyr interval, only two higher SST values are observed: one at 6.82 Ma and another one at 6.75 Ma. Between 6.69 and 6.54 Ma, corresponding to the upper part of the section, SST shows pronounced variability. The TEX^{H}_{86}-SSTs values increase from 22.6 °C to more than 28 °C with a visible cyclic pattern and 3 to 4 °C amplitude between colder and warmer phases (Fig. 3A).

$U^{K}_{37}{}'$-SSTs show the least variability (23.7 to 28.2 °C) averaging around 26.9 °C (Figs. 3A, 4D; Supplementary table). If we discount the sample at 7.1 Ma, then the $U^{K}_{37}{}'$-SST average increases to 27 °C, with a variation of only 3.3 °C. Alkenones were present in 24 out of the total 47 samples analyzed and the low variation could be caused by the lower amount of U^{K}_{37}-SST values obtained (Figs. 3A, 4D; Supplementary table). However, for the 24 levels where SST estimates based on both TEX^{H}_{86} and $U^{K}_{37}{}'$ were available the obtained values are closely reproduced (Figs. 3A, 4D; Supplementary table). It is noteworthy that, especially during cooler episodes as described by TEX^{H}_{86}-SSTs, fewer levels with alkenone occurrence were identified and therefore, less $U^{K}_{37}{}'$-SSTs are available in the Agios Myron section (Figs. 3A, 4D).

4.2. Oxygen stable isotopes on Globigerinoides obliquus

Over the analyzed record, *G. obliquus* $\delta^{18}O$ values show an average of −0.08‰, with a minimum of −1.61‰ at 6.58 Ma and a maximum of 0.99‰ at 6.80 Ma (Fig. 3B; Supplementary table). The largest variability based on the standard deviation of the replicates is ~0.5‰. From the base of the section to ~6.95 Ma, $\delta^{18}O$ values display considerable scatter from 0.75 to −1.22‰, with the majority having negative $\delta^{18}O$ values. In the cyclically-bedded interval, the planktonic $\delta^{18}O$ record correlates well with lithology, with lower $\delta^{18}O$ values occurring within sapropels, reflecting wet climatic conditions at times of minimum precession (Rohling et al., 2015). Less variable and rather higher $\delta^{18}O$ values are generally observed in the middle part of the section (~6.95–6.69 Ma). Within this interval, we observe significant increases in $\delta^{18}O$ values at ~6.93, 6.82, and 6.80 Ma, and corresponding decreases at ~6.97, 6.85 and 6.76 Ma. The shift towards higher $\delta^{18}O$ values culminates about 6.7 Ma, where $\delta^{18}O$ values stabilize around 0.5‰. From this level towards the top of the section, a recovery to slightly lower values (around 0‰) is observed, except for the negative peak with the lowest value of the entire record (−1.61‰) at ~6.59 Ma (Fig. 3B; Supplementary table).

Following the results of previous studies on the Mediterranean Sea (Kontakiotis et al., 2016, 2019; Vasiliev et al., 2019), we also use $\delta^{18}O_{IVF\text{-}SW}$ as a direct method of isotopic tracing of eastern Mediterranean (hyper)saline events, since SST has been removed, leaving primarily a salinity signal in the $\delta^{18}O_{IVF\text{-}SW}$. There is a remarkable coincidence for both $\delta^{18}O_{IVF\text{-}SW}$ and SSS records (Figs. 3C, D) with distinct positive and negative excursions that reveal successive hypersaline and freshening events during the Messinian, described in detail in section 4.3.

4.3. Salinity reconstruction

Estimated SSS data at Agios Myron range from 36.6 to 47.9, and 37.1 to 47.5 based on the contribution of TEX^{H}_{86}- and $U^{K}_{37}{}'$-SSTs, respectively (Figs. 3D, 4B; Supplementary table). The SSS based on both TEX^{H}_{86}-SSTs and $U^{K}_{37}{}'$-SSTs have strikingly similar amplitudes (~11 or 10, respectively). Remarkably, regardless of the choice of TEX^{H}_{86}-SSTs or $U^{K}_{37}{}'$-SSTs, maximum SSS values attain 47 to 48, typical of hypersaline conditions (Figs. 3D, 4B; Supplementary table).

Overall, the studied interval at the base of the section shows that hypersaline conditions that developed during the latest Tortonian (39.5 to 43.9, average 41.7; Kontakiotis et al., 2019), persisted immediately above the Tortonian/Messinian boundary (40.6–45.8, average 42.2 based on TEX^{H}_{86}-SSTs). Subsequently, the data document a freshening trend up to 6.95 Ma. The SSS values based on both TEX^{H}_{86}-SSTs and $U^{K}_{37}{}'$-SSTs display a remarkable decline up to average of 38 and average of 36.6 respectively, indicating a brief, but gradual passage from hypersaline to saline and finally to normal marine conditions. The interval between 6.95 and 6.69 Ma indicates hypersaline surface water conditions in the eastern Mediterranean (39.4 to 47.9, average ~43.5 based on TEX^{H}_{86}-SSTs and 39.2 to 47.5, average 43.5 based on $U^{K}_{37}{}'$-SSTs), regardless of the choice of SST proxy. From 6.95 to 6.69 Ma, salinity increases systematically documented through a succession of five pronounced events of variable duration and magnitude (Figs. 3D, 4B). We separate these events into three primary and two ancillary ones. The primary events are defined by a wider amplitude and duration, while the ancillary ones as those SSS increase appearing instantly. The first primary event occurred between 6.87 and 6.85 Ma. The second event, centered at 6.82 to 6.80 Ma, was equally brief but even more saline than the first, while the third one appears as equally large in amplitude but with a more persistent (6.72 to 6.69 Ma) salinity phase. All these primary events seem to be separated by short pauses (with fresher but still hypersaline conditions) highlighting the high-frequency salinity variability through the Messinian. Following the high salinity interval between ~6.95–6.69 Ma, we observe a freshening towards the top of the record. However, for the 6.69–6.54 Ma interval a large variation in salinity (between 37.3 and 47.7; SSS based on TEX^{H}_{86}-SSTs) is observed (Figs. 3D, 4B; Supplementary table).

5. Discussion

5.1. Errors and uncertainties on applied temperature and salinity proxies

Overall, the most significant source of error is our normalization-to-modern approach, which typically concerns all past sea surface temperature and salinity-related reconstructions. Regarding the temperature estimates, a significant limitation are possible seasonal offsets on the $\delta^{18}O$ and temperature signals due to growth and habitat differences between the planktonic foraminifera (*G. obliquus*) on one side, and Thaumarchaeota, producing isoGDGTs, and coccolithophoriids, the alkenone-producing haptophyte algae on the other side.

Both biomarker-based TEX_{86} and $U^{K}_{37}{}'$ temperature proxies assume growth temperature (i.e., SST) as the main factor affecting the composition of the corresponding lipids. However, other factors like growth rate, nutrient levels, environmental stress and regional oceanographic conditions may play an unaccounted role in the lipid composition and, therefore, the resulting SST estimates (e.g., Leider et al., 2010; Elling et al., 2019). Recent studies from the modern Mediterranean basin warn about a possible bias in the TEX_{86} paleothermometer from deep-dwelling marine archaea, showing a different GDGT membrane composition than epipelagic archaea (Kim et al., 2015; Besseling et al., 2019). However, the isoprenoidal GDGT2/GDGT3 ratios (Supplementary Fig. 2) in the Agios Myron section are typical for input from the upper water column in the present-day eastern Mediterranean (Kim et al., 2015). Alkenone paleothermometry ($U^{K}_{37}{}'$-based SST) appears more suitable/less biased in the Mediterranean Sea (Herbert et al., 2016); however, these alkenones were produced by extinct species of haptophytes (Herbert et al., 2016; Tzanova et al., 2015), a fact imposing a certain degree of uncertainty in all paleo-SST reconstructions. The exact alkenone producers are not known for the Agios Myron section. We infer that the most probable alkenone producers in the Agios Myron section would have been *Coccolithus pelagicus*, "normal sized" reticulofenestrids (including *Reticulofenestra haqii*, *R. pseudoumbilicus*) as

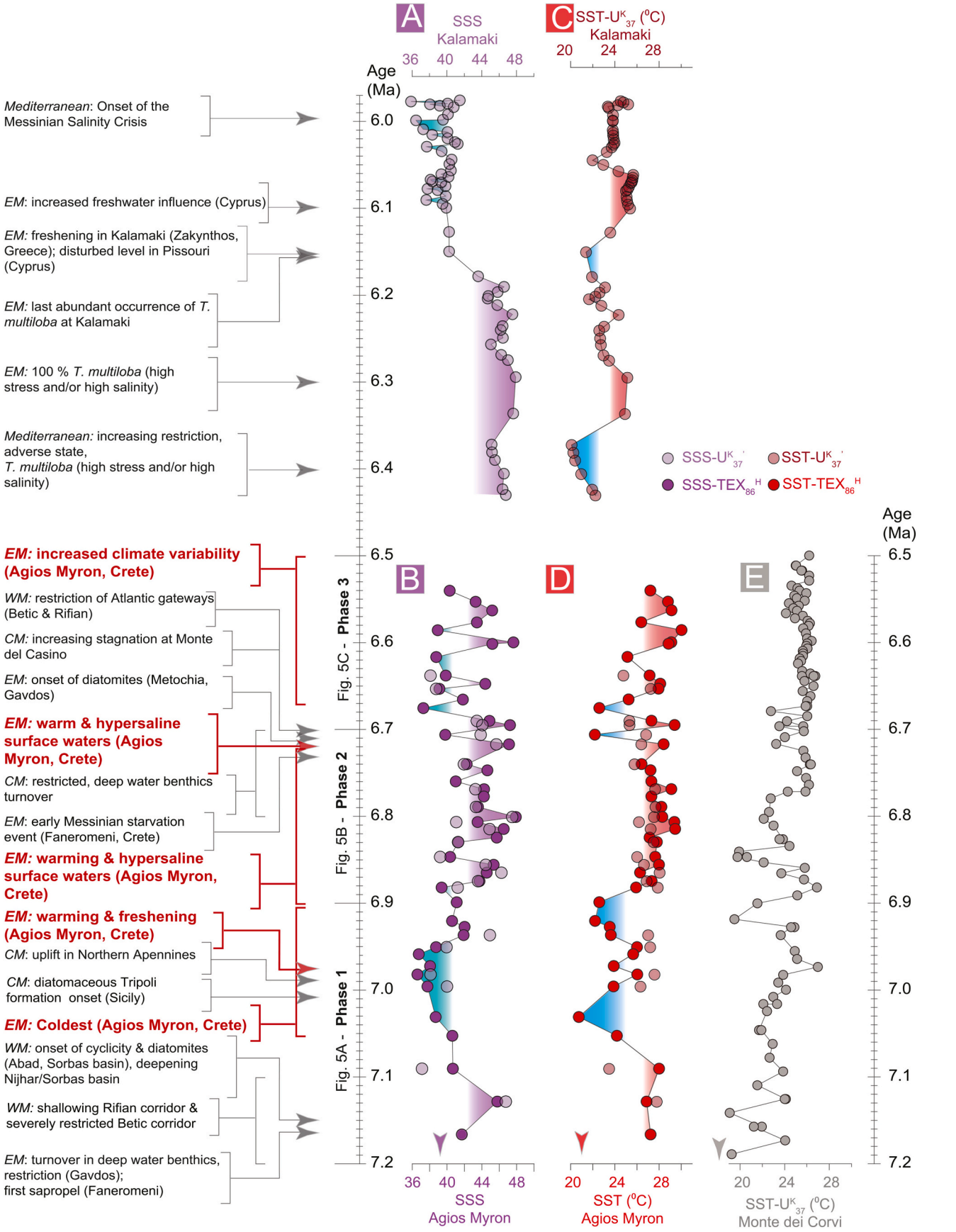

(caption on next page)

Fig. 4. Messinian SST and SSS data from Mediterranean between 7.17 and 5.96 Ma. The events affecting different parts and periods of the Mediterranean are compiled from: Hilgen and Krijgsman (1999), Kouwenhoven et al. (1999, 2003, 2006), Blanc-Valleron et al. (2002), Sierro et al. (2001); Gennari et al. (2018), Krijgsman et al. (2018) and Vasiliev et al. (2019). In bold red are events revealed by this study. EM, CM and WM stand for eastern, central and western Mediterranean, respectively. Composite SSS of the eastern Mediterranean with data from A) Kalamaki Section (Zakynthos Island; Vasiliev et al., 2019) for the interval between 6.46 and 5.96 Ma, and B) our data from Agios Myron (Crete) for the interval between 7.17 and 6.54 Ma. The arrow indicates the present-day SSS; Composite SST of the eastern Mediterranean from C) Kalamaki (SST-U^{K}_{37}') and D) Agios Myron (SST-TEX^{H}_{86} and SST- U^{K}_{37}') sections. The arrow indicates the present-day SST at Agios Myron location; E) SST-U^{K}_{37} from Monte dei Corvi (Italy) from 7.2 to 6.4 Ma (Tzanova et al., 2015). The arrow indicates present-day SST at Monte dei Corvi location. (For interpretation of the references to colour in this figure legend, the reader is referred to the web version of this article.)

documented from the closest, time-equivalent record from Pissouri (Cyprus; Kouwenhoven et al., 2006).

As we have no means to estimate the slope of the $\delta^{18}O_{sw}$–S relationship for the late Miocene, we used the modern relationship for the Mediterranean Basin (Pierre, 1999). Paleosalinity estimates assume that the $\delta^{18}O_{SW}$-S relationship is constant through space and time (i.e., spatiotemporal stationarity). Overall, future work requires more robust knowledge about these parameters through both upgraded records of SST proxies for the eastern Mediterranean Sea and the development of a conservative $\delta^{18}O_{sw}$–S relationship under changed past climatic conditions.

We estimate the ±1σ uncertainty on calculated $\delta^{18}O_{SW}$ values to be ~0.38‰ based on the propagation of the 1σ analytical error on *G. obliquus* $\delta^{18}O$ values and the pooled standard deviation value of our SST replicates with the reported errors on the calibration equations of Müller et al. (1998) and Bemis et al. (1998). Absolute errors in $\delta^{18}O_{IVF\text{-}SW}$ are difficult to assess for the late Miocene, but are expected to be of minor importance as changes in global ice volume were small during this time interval and do not alter the relative changes between records (Williams et al., 2005). The propagated error suggests uncertainties of ~1.3 for Messinian salinity values, in accordance with previous reconstructions (Mehta et al., 2021).

Acknowledging the possible bias associated to the palaeothermometry applications in increasingly old and undeciphered records, the parallel application of TEX_{86} and U^{K}_{37}' temperature proxies in conjunction with the standard assumption that the $\delta^{18}O_{SW}$-S relationship is constant through space and time, came as a viable solution in our attempt for obtaining the SSS estimates in the eastern Mediterranean during the early Messinian at an unprecedent time-resolution. Given that the obtained TEX^{H}_{86}-SSTs values are closely reproduced at 24 available levels by U^{K}_{37}'-SSTs (Figs. 3A, 4D) we are safely encouraged to use the TEX^{H}_{86}-SST and U^{K}_{37}'-SST values for the further SSS calculations (Figs. 3D, 4B) and subsequent discussion.

5.2. SST variability

The reconstructed Agios Myron temperature estimates generally exceed the modern mean annual SST of ~21 °C (at the site) by as much as 5.7 °C (Figs. 3A, 4D), consistent with higher global temperatures for that time (e.g., Herbert et al., 2016). Additionally, for both TEX^{H}_{86}- and U^{K}_{37}-SSTs, the ≤4–5 °C amplitude of SST change between warmer and colder periods within the 7.2–6.5 Ma time interval (Figs. 3A, 4D) is smaller than the 8–9 °C glacial-interglacial variation recorded in the Mediterranean Sea during late Quaternary (Emeis et al., 2000). Surprisingly, the TEX^{H}_{86}-SSTs correlate well with the insolation curve (Fig. 3A), although orbital tuning was not our initial target as we collected two samples per lithological cycle only. For the basal seven meters (~7.2–7.05 Ma), we refrain from firmly matching the TEX^{H}_{86}-SSTs to the insolation curve because the age constraints here are limited to the assumption of constant sedimentation rate for the five samples. However, samples AM 25, AM 24 and AM 23 indicate warm Mediterranean surface waters (~27 °C) and all three samples fit to warm insolation peaks (Fig. 3). For the first cyclic part (7.05–6.9 Ma) the TEX^{H}_{86}–SSTs record shows highest values at AM 19 (6.96 Ma), coinciding with one of the highest peaks in insolation (Fig. 3). Afterwards, the cooling around 6.92 Ma (AM 17) and 6.90 Ma (AM 16C) coincide with minima in the insolation curve. The 6.9 to 6.7 Ma interval is characterized by low-amplitude precession influencing the insolation values. This feature is recorded in the TEX^{H}_{86}-SSTs as a long period of low variation albeit at high SST values (28 °C). In the youngest part of the record, the TEX^{H}_{86}-SSTs show large variability, likely induced by increased fluctuations in the insolation curve (Fig. 3A). The high SST values at 6.65 Ma (AM 05) and 6.59 Ma (AM 02) correspond to the highest insolation values, whereas the 6.62 Ma (AM 03C) low value coincides with an insolation minimum.

5.3. SST comparison to other Mediterranean Messinian records

The calculated TEX^{H}_{86} and U^{K}_{37} SST range covers realistic values throughout the 7.2 to 6.5 Ma interval (Figs. 3A, 4D; Supplementary table), comparable to the previously reported late Miocene U^{K}_{37}-based SSTs from Monte dei Corvi (Fig. 4E; northern Italy; Tzanova et al., 2015) and Kalamaki (Fig. 4C; Zakynthos Island, Greece; Vasiliev et al., 2019). Although the different sampling resolution does not allow a detailed comparison among the reconstructed SST records, they show a comparable general trend with only some discrepancies between the SST ranges during the Messinian (Figs. 4C-E). Tzanova et al. (2015) report SSTs between ~19.5 and 27.5 °C (Fig. 4E), slightly lower than the equivalent U^{K}_{37}' estimates between ~23.7 and 28.2 °C for Agios Myron (Fig. 4D). This apparent discrepancy can be accounted for by the ~10° difference in paleolatitude between the Monte dei Corvi and Agios Myron sections (Fig. 1).

TEX^{H}_{86}-based SST estimates were not used until now for the pre-MSC interval and therefore direct comparison to equivalent Mediterranean records is impossible. However, the TEX^{H}_{86}-SSTs reproduce well the high values of the U^{K}_{37}'-SSTs obtained for Agios Myron. When analyzing the TEX^{H}_{86}–SSTs record, in the lower part of the Agios Myron section (~7.2–6.9 Ma), a shift towards 8 °C cooler conditions at 7.03 Ma is hardly recognizable within Monte dei Corvi U^{K}_{37}-SST estimates. There is only a ~ 2 °C decrease in Monte dei Corvi, but to values that are similar to Agios Myron TEX^{H}_{86}-SSTs (20–22 °C). At 6.88 Ma, the TEX^{H}_{86}-SST shows a prominent decrease by 4 °C to 22 °C, similar to the 5 °C decrease to 19.5 °C at Monte dei Corvi (Tzanova et al., 2015). Agios Myron $TEX_{86}{}^{H}$-SSTs do not capture the terminal cooling event observed in the high-resolution Monte Dei Corvi record at ~6.85 Ma, possibly due to the lower resolution of our sampling pattern. However, for certain time intervals the $TEX_{86}{}^{H}$ paleothermometer records even higher temperatures as evidenced in the very warm (28.7–29.8 °C) interval documented at 6.81–6.80 Ma. In such cases, where the U^{K}_{37} index approaches the paleothermometers' limit of 1 (i.e., exclusive presence of $C_{37:2}$ alkenone), we succeed to avoid the underestimation of the magnitude of warmth by using $TEX_{86}{}^{H}$. In the upper part of the section (~6.8–6.5 Ma), we observe a rather large spread of values ranging from 22.6 °C to more than 28 °C (Fig. 4D). In contrast to the rather stable, yet high SSTs around 24–25 °C at Monte dei Corvi (Fig. 4E), the 6.8–6.5 Ma part of the Agios Myron record depicts a generally warm environment, but punctuated by colder peaks at 6.68, 6.62 and (less at) 6.57 Ma (Fig. 4D). There is evidence from both Zakynthos (Kalamaki section; Fig. 4C; Vasiliev et al., 2019) and Cyprus (Pissouri section; Mayser et al., 2017) that this variable temperature pattern continued until ~6.0 Ma.

5.4. Messinian sea surface salinity in the Mediterranean

The reconstructed long-term variability in SSS estimates of 36.6 to

47.9 exceeds the standard error of the measurements (Figs. 3D, 4B; Supplementary table). The SSS estimates are within the modeled range for the Mediterranean during the pre-evaporitic Messinian stage (Simon et al., 2017). The calculated values for the 7.2–6.5 Ma interval at Agios Myron indicate that the Mediterranean basin was characterized by hypersalinity for a significant amount of time, reaching almost 48 (Fig. 4B). Yet, the values obtained here are similar to the calculated $U^{K}_{37'}$-SSTs-derived SSS estimates of maximum of 47.9 (at 6.42 and 6.15 Ma) obtained in the eastern Mediterranean pre-evaporitic Kalamaki section (Fig. 4A; Vasiliev et al., 2019). The SSS values from Agios Myron are higher than the Sr/Ca-derived SSS estimates for the 7.16–6.93 Ma time interval, but reach equal values of 38 at 6.98 Ma (Kontakiotis et al., 2019). Discrepancies on the SSS estimates may arise from the different proxies used for SST determination (i.e., biomarker- vs. foraminifera-based) and the application of different linear $\delta^{18}O_{SW}$-S relationships (i.e., differential slopes and intercepts) in these studies depending on the latitudinal position of the analyzed sections and the salinity range coverage (i.e., increase of evaporation from west to east, regional freshwater input). Through this comparison, the analyzed settings exhibit a strong variability in slopes and appear to be specific for the region, ranging from 0.48 (westernmost Alboran Sea; Laube-Lenfant, 1996) to 0.41 (southwestern Mediterranean for $S < 38$; Kallel et al., 1997) to 0.25 (entire Mediterranean basin for $S > 36.2$; Pierre, 1999) and finally to 0.199 (northwestern and eastern Mediterranean for $S > 37.5$; Kallel et al., 1997). The shallower slope observed in the eastern Mediterranean surface waters likely results from higher evaporation rates in eastern Mediterranean basins relative to the west, shifting the higher salinity water masses to higher oxygen isotopic values. Across the existing datasets, we selected that of Pierre (1999), as the most representative for the study area, covering a wide oceanic salinity range with salinities exceeding 36.2. Beyond the above SSS reconstructions, there are also sparse reports for hypersaline conditions in Mediterranean Messinian for specific (short) time intervals (e.g., 6.74 Ma – Zachariasse et al., 2021; Zachariasse and Lourens, 2021; 6.71 Ma – Blanc-Valleron et al., 2002; 6.68 Ma – Santarelli et al., 1998), further reinforcing our findings of high salinity values in Agios Myron. Overall, considering all these references for enhanced salinity in the eastern Mediterranean Basin throughout the Messinian, we point out that the transition from normal marine to hypersaline conditions started at ~6.9 Ma, well before the initial observations of ~6.3 Ma (Bellanca et al., 2001; Blanc-Valleron et al., 2002), constraining in this way the stepwise evolution towards hypersaline conditions during the earliest Messinian, apparent in upper bathyal settings like the Heraklion Basin of Crete.

5.5. *Hydro-climatic changes before the onset of the MSC*

The prolonged late Miocene cooling (~7.4–5.4 Ma) is associated with changes in atmospheric and oceanic circulation, which have been documented both within the subtropical Mediterranean basin (between 7.2 and 6.7 Ma; Kontakiotis et al., 2019; Tzanova et al., 2015) and globally in all oceans (e.g., between 7.1 and 5.4 Ma at tropical and mid- to high-latitude regions; Herbert et al., 2016). However, in the Mediterranean region the detailed sequence of climatic events and the range of related hydrologic variability through that period remain poorly understood. Importantly, the paleogeography of the Mediterranean region, the restriction and partial closure of the western Mediterranean corridors impose a different dynamic of the water circulation within the basin. Such connectivity and hydrological changes revealed the recognition of evolutionary steps related to distinct paleoenvironmental phases, which developed gradually in a stepwise fashion in western (Sierro et al., 2003; Corbí et al., 2020; Bulian et al., 2021), central (Blanc-Valleron et al., 2002; Di Stefano et al., 2010) and eastern (Kouwenhoven et al., 1999, 2003, 2006; Gennari et al., 2018; Zachariasse et al., 2021; Zachariasse and Lourens, 2021) Mediterranean basins. The SST and SSS patterns revealed here provide context for a development in three consecutive phases (Figs. 5A-C). Its stepwise character, evidenced

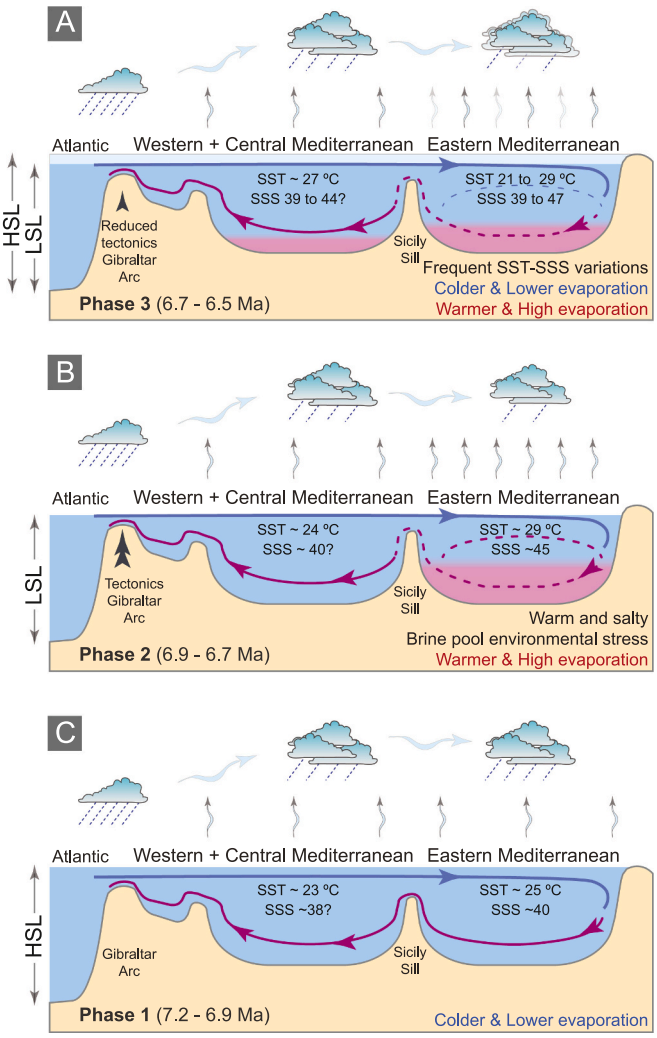

Fig. 5. Schematic representation of the environmental conditions during important hydrologic changes in the early part of the Messinian Mediterranean Sea. A) During Phase 1, Mediterranean experienced coldest times under close to normal saline conditions; B) during Phase 2, pronounced warming and hypersalinity appear, with possible salinity driven stratification of the water column in the eastern Mediterranean; and C) during Phase 3 intensification of climate and salinity variability, accompanied by enhanced stratification of the water column.

by significant SST and SSS perturbations, highlights the presence of a transitional interval preceding the MSC. The concurrent progressive gateway restriction taking place in the western basin and the advent of hydrological changes from open marine to sluggish and hypersaline conditions in the eastern Mediterranean reflect a synergy between tectonics and climate during that period. However, the amplitude and relative importance of these drivers for specific time intervals are still a matter of discussion.

5.5.1. *Phase 1: ~7.2–6.9 Ma – open marine conditions during the start of the Messinian cooling*

The oldest part of Agios Myron record exhibits a gradual transition from hypersaline to saline and finally to open marine conditions with TEX^{H}_{86}-SSTs fluctuating by 7 °C between 20.7 and 28 °C and SSSs varying between 36.6 and 45.8, with an average of 40.0 (Fig. 5C). Phase 1 includes a two-step cold episode punctuated by a rebound to higher temperatures. The lower part of phase 1 (~7.21–7.05 Ma) corresponds to silty marls without sapropels followed by cyclic deposition of 7 marl/sapropel couplets (~7.05–6.90 Ma). During this latter interval, the

coldest excursions to 20.7 °C and 22.2 °C occurred at 7.03 and 6.91 Ma, respectively (Fig. 3A). In between these minimum values, the average SST rebounds to ~26 °C (Fig. 3A), which is close to the average SST recorded around the Tortonian/Messinian boundary (~25 °C, Kontakiotis et al., 2019; Tzanova et al., 2015). These minima at 7.03 and 6.91 Ma fall within the relevant brief cooling period of ~7.1–6.9 Ma, when a strong SST decrease (~9 °C) was recorded in the nearby Cretan Faneromeni section (Kontakiotis et al., 2019). Although there was no evidence of termination of this cooling trend in Faneromeni due to the observed diagenetic bias in Sr/Ca-SST after 6.9 Ma, the data from Agios Myron clearly place the end of the cooling in the eastern Mediterranean at 6.9 Ma, when a warm and hypersaline water column starts to develop ($\delta^{18}O_{IVF\text{-}SW}$ around 3 and SSS > 41; Figs. 3C, D and 4B). Cooling and evaporation of the circum-Mediterranean basin at about 7.0 Ma are also supported by enhanced dust accumulation rates (e.g., Sahara dunes; Schuster et al., 2006), noticeable planktonic and benthic carbon isotopes shift towards lighter values (Late Miocene Carbon Isotope Shift; Kontakiotis et al., 2019; Bulian et al., 2022) related to increased aridity (e.g., Hodell et al., 1994) and vegetation changes towards more C_4 plant contribution (e.g., Uno et al., 2016) leading to the expansion of open habitats that could have invigorated eolian transport over the Mediterranean subsequently inducing increased silica contribution (Pellegrino et al., 2018) as visible from the diatomite rich layers accumulating from 7.17 Ma in the Sorbas Basin or in the Tripoli formation in Sicily (e.g., Hilgen and Krijgsman, 1999; Roveri et al., 2014; Sierro et al., 2003). We further note that the warmer period within phase 1 at 6.97 Ma is accompanied by fresher surface water ($1 < \delta^{18}O_{IVF\text{-}SW} < 2$ and SSS < 40; Figs. 3C, D and 4B), typical for the upper Miocene and Pliocene Mediterranean paleoceanography.

5.5.2. Phase 2: 6.9–6.7 Ma – enhanced restricted conditions and environmental stress due to increased temperature and salinity

From 6.9 to 6.7 Ma, the marine conditions changed significantly, with surface waters characterized by elevated temperatures and salinities, most likely associated with the progressive restriction of the Mediterranean basin (Fig. 5B). At the beginning of phase 2 (6.87–6.81 Ma), excursions to positive $\delta^{18}O_{IVF\text{-}SW}$ (i.e., saltier) and subsequent high SSS values (40.4 to 46.5) suggest hypersaline sea surface conditions, which are consistent with observations in the Sicilian basin (e.g., Marianopoli section; Bellanca et al., 2001). Faunal development (reduction of benthic diversity and dominance of salinity-tolerant species) and geochemical (Mn/Al, V/Al) parameters from several central and eastern Mediterranean sections (Falconara/Gibliscemi, Monte del Casino, Metochia, Pissouri) further point towards intermittent periods of severely stressed benthic faunal communities around 6.8 Ma (Drinia et al., 2007; Kouwenhoven et al., 1999, 2006). This period of increased environmental stress coincides with the highest salinity (47.9) in the Agios Myron record (Fig. 3D, 4B; Supplementary table). Declining foraminiferal diversity and mass occurrences of phytoplankton adapted to high salinity throughout the Mediterranean are all evidence of increasing salinity stress (Kouwenhoven et al., 1999; Santarelli et al., 1998; Sierro et al., 2003). Although planktonic foraminiferal growth was progressively inhibited as a consequence of the subsequent high salinity (this study; Zachariasse et al., 2021; Zachariasse and Lourens, 2021), the reconstructed values remain within their tolerance ranges (Bijma et al., 1990) and below the relevant paleoecological thresholds (< 49; Fenton et al., 2000). Reconstructed SSTs from Agios Myron are ~28 °C (Figs. 3A, 4D), thus confirming the dual character (thermal and salinity increase) of environmental stress over this interval. This pronounced warm and salty interval was interrupted by a rebound to relatively lower SSSs (40.4) under persistent warm conditions at 6.85 Ma (Figs. 3D, 4B). The same hydrological regime was maintained until 6.72 Ma, where an abrupt and brief high-salinity event (SSS = 47.2) is documented in Agios Myron (Figs. 3D, 4B). During this interval, temperature and salinity increase concomitantly. The extremely warm and saline surface waters, possibly due to their restricted outflow, indicate the reduction of the Atlantic influence over the Mediterranean Sea. This result is further supported by age-equivalent changes in Messinian gateway restriction (Krijgsman et al., 2018). Increasing isolation of the Mediterranean due to tectonics and/or eustacy may have led to increased residence times of water masses within the basin (e.g., Abad – Sierro et al., 2003; Agios Myron – Zachariasse et al., 2021; Gavdos – Zachariasse and Lourens, 2021) and in combination with warming (this study) the slow-down of thermohaline circulation and enhancement of water column stratification as supported by the increased difference between benthic and planktonic $\delta^{18}O$ values (Zachariasse and Lourens, 2021). Given that sensitivity of a basin to the variation of the surface heat decreases with increasing size of the gateway (Flecker et al., 2015; Karami et al., 2011) we conclude that during phase 2 the strongest response of salinity to hydro-climate variability reflects even smaller marine gateways. According to our data, this occurred at 6.72 Ma, 20 kyr later than the significant increase in $\delta^{18}O$ values in both benthic (0.7‰) and planktonic (0.5‰) foraminifera in Agios Myron (Zachariasse et al., 2021) as well as in other sections (e.g., average 1.72‰ and 0.97‰ $\delta^{18}O$ increases in Gavdos; Zachariasse and Lourens, 2021) along the Mediterranean Sea. The Mediterranean-wide character of this event could be another evidence for gateway restriction, with its amplitude varying with location. Such gateway configuration changes (dimensions, bathymetry and geometry) as well as their control on Mediterranean water properties have been proposed by several studies (e.g., Blanc, 2006; Ivanovic et al., 2014; Meijer, 2012). For instance, Simon and Meijer (2015) indicated that Atlantic-Mediterranean exchange during the deposition of the Primary Lower Gypsum was as low as 10 to 25% when compared to the present-day value at the Strait of Gibraltar, while Krijgsman et al. (2018) estimated that longer and narrower straits existed at greater water depth. Therefore, we hypothesize that the gateway configuration and evolution through the Messinian acted as a key factor for the hydrological change reflected in phase 2 in the Agios Myron (this study, Zachariasse et al., 2021) and Gavdos sections (Zachariasse and Lourens, 2021), and such local effects (both restriction and hydrology related) prevail over the global cooling.

5.5.3. Phase 3: 6.7–6.5 Ma – continuous warming, intense salinity fluctuation, enhanced basin stratification

The upper part of the Agios Myron section clearly demonstrates a distinct colder episode during the long-term warming trend with high-amplitude variability between ~6.7–6.5 Ma (Figs. 3A; 5A). This ~0.2 M.y. excursion starts at 6.7 Ma with a sharp drop in SST from 27 °C to 22 °C, followed by a recovery to 28 °C at 6.66 Ma and a second drop to 24 °C around 6.61 Ma (Figs. 3A; 4D). This variable pattern continues to 6.54 Ma with additional SST maxima and minima. Similarly, both $\delta^{18}O$ and reconstructed SSS present a strikingly variable pattern, reflecting the evolution towards an environment mostly characterized by hypersaline conditions (positive $\delta^{18}O_{IVF\text{-}SW}$ shifts and/or maximum SSS values) with some freshening episodes (negative $\delta^{18}O_{IVF\text{-}SW}$ shifts and/or minimum SSS values) (Figs. 3C, D). In this interval the cyclic pattern is obvious in the Agios Myron section.

Similar variations of the depositional environment were reported throughout the eastern Mediterranean because of its more restricted configuration compared to the western basin. Dinocyst data from the Faneromeni section indicate hypersaline surface waters at 6.68 Ma (Santarelli et al., 1998), and combined benthic foraminifera faunal and geochemical data from the study section as well as the nearby Metochia section further show permanent hypersaline deep-water conditions after 6.74 ± 0.04 Ma (Zachariasse et al., 2021; Zachariasse and Lourens, 2021). It is worthy to note that such salinity change lag between deep- and surface-waters is not well understood yet and requires further investigation. Moreover, the first diatomites at Gavdos appear at 6.72 Ma (Drinia et al., 2007; Zachariasse et al., 2021), time when the western Mediterranean sedimentation changes to alternation of sapropels and homogeneous marls with irregularly intercalated diatomites (Roger et al., 2000; Cornée et al., 2002). The fact that SSS values strongly

fluctuate in phase 3 while deep water remains hypersaline could be explained by occasional freshwater inputs, because the hypersaline subsurface water mixes less well and therefore runoff should have a clear effect on sea surface salinities. Regarding the potential source of these freshwater inputs, recent observations from Cyprus (Mayser et al., 2017) suggest a stronger dilution by continental waters from runoff (both from North Africa and Anatolia Plateau catchments) rather than an increase of oceanic inputs. This inflow of less saline surface waters, together with the persistence of strongly saline intermediate and hypersaline deep waters of the marginal eastern Mediterranean basin could have caused a strong stratification in the water column, preventing bottom ventilation and favoring sapropel formation.

5.6. Tectonic versus climatic drivers on the Messinian evolution of the MSC

During the Tortonian/Messinian boundary, the open Atlantic-Mediterranean exchanges maintained relatively stable marine conditions, expressed through a relatively cool and fresh upper water column for the eastern Mediterranean (Kontakiotis et al., 2019). The reduction in efficiency of gateways between the Atlantic Ocean and the Mediterranean Sea started at about 7.2 Ma (initial stage of the Late Miocene cooling) because of the tectonic uplift of the Rifian and Betic corridors (Kouwenhoven et al., 1999; Krijgsman et al., 1999b). Tectonic control was likely to be dominant during the earliest Messinian (phase 1; 7.2–6.9 Ma; Fig. 5C) since all known gateways (through Morocco and Spain) were closed around this time except for a long, narrow channel at Gibraltar (Krijgsman et al., 2018). Although the possibility of the existence of a proto-Gibraltar strait as the main source of Atlantic inflow in the earliest Messinian has been multidisciplinary surveyed based on foraminiferal and sedimentological records (El Achalhi et al., 2016; Bulian et al., 2021) and computational reconstructions (Krijgsman et al., 2018), further investigations are needed to be completely validated. Shallower gateways caused higher temperatures and salinities in the upper water column, whereas the reduction of the vertical circulation led to bottom water stagnation or at least to significant circulation slowdown. In Agios Myron, SST increases at ~6.95 Ma, while SSS follows at ~6.9 Ma. During the salinity increase identified in the eastern Mediterranean from 6.9 to 6.7 Ma, faunal diversity decreased (less diversified planktonic faunas dominated by two or three species; Zachariasse et al., 2021) as conditions deteriorated once the oceanic link was weakened (Zachariasse and Lourens, 2021). As a result, the eastern Mediterranean basin turned into a warm and hypersaline pool with increased environmental stress (phase 2; Fig. 5B). Additionally, the Sicily channel may have limited the connections between the western and the eastern Mediterranean (Bialik et al., 2021) amplifying the differences in basin conditions (Gladstone et al., 2007). The termination of elevated SST and SSS recorded at 6.72 Ma was further accompanied by a change in the processes governing surface water productivity controlling the onset of the diatomite deposition on Gavdos Island (Zachariasse et al., 2021).

Phase 3 (6.7–6.5 Ma; Fig. 5A), characterized by large fluctuations of SST and SSS under dominant climate control, can be considered as the transition from the initiation of hypersalinity (at ~6.9 Ma) to the onset of the MSC marked by deposition of subaqueous evaporites. The cooling at 6.68 Ma was accompanied by enhanced water column stratification that lasted over the entire phase 3, as supported by increased difference in the oxygen isotopic values between benthic and planktonic foraminifera from both Agios Myron (Zachariasse et al., 2021) and Gavdos (Zachariasse and Lourens, 2021). SSS fluctuations and increasingly stagnating bottom waters at 6.7 Ma in the eastern and central Mediterranean along with the reduction in terrigenous supply in the eastern Mediterranean (Blanc-Valleron et al., 2002; Kouwenhoven et al., 2006; Santarelli et al., 1998) were consequences of restrictions along the Betic and Rifian corridors (e.g., Sierro et al., 2001; van Assen et al., 2006; Hüsing et al., 2009). These short-term climatic fluctuations induced strong changes in the SSS (from high saline to diluted conditions), evident especially at times of increased continental input during summer insolation maxima resulting in a dilution of the surface waters responsible for the subsequent density driven stratification of the water column.

6. Conclusions

The Agios Myron section (Crete) contains a key sedimentary succession with marl-sapropel cyclicity to assess the hydroclimatic conditions prior to the onset of the MSC. The presented geochemical (biomarker and oxygen isotope) data indicate that the stratigraphic interval from 7.2 to 6.5 Ma, approximately 0.5 Myr before the onset of the MSC, is characterized by high-frequency SST and SSS oscillations whose amplitude strongly exceeds those of the global oceans. Overall, these oscillations are in phase with precession, indicating a solar insolation as the primary driver, with subordinate controls through tectonic and glacio-eustatic processes. During the pre-evaporitic Phase 1 (7.2–6.9 Ma), however, it is likely that tectonic activity caused restriction and reduced Mediterranean circulation with climate forcing superimposed on the stepwise evolution of the basin. In particular, the observed temperature and salinity variability recorded in the Agios Myron section provides evidence of fluctuating and increasing environmental stress, in accordance with the stepwise restriction of the eastern Mediterranean Basin preceding the deposition of evaporites. After the beginning of the Messinian, the open Atlantic-Mediterranean exchanges maintained relatively stable marine conditions, expressed through a relatively cool and fresh upper water column for the eastern Mediterranean. At ~6.9 Ma, the onset of Phase 2, the combined effect of a larger water deficit and/or the abrupt isolation of the Mediterranean Basin at a greater and probably faster pace (also related to the mode of gateway flow as a result of the passage configurations) led to the development of a hypersaline warm pool. An important increase in heat flux highlights a warm double-peak centered at 6.9–6.8 and 6.72 Ma, which is attributed to thermal and salinity stress, respectively. In between, the freshening event recognized at 6.8–6.7 Ma indicates that the Mediterranean Sea episodically experienced fully marine connections to the Atlantic Ocean, possibly related to the variation in volume periodic overflow (e.g., the Sicilian sill). Phase 3, between 6.72 and 6.54 Ma, was characterized by a wide range, precession-scale sea surface temperature and salinity fluctuations. Increased continental inputs in the North African and Anatolian Plateau riverine runoff, resulted in the freshening of surface waters – now quantified in this study – and led to the reduction of the vertical circulation and enhanced water column stratification during warm intervals.

Declaration of Competing Interest

The authors declare the following financial interests/personal relationships which may be considered as potential competing interests:

Iuliana Vasiliev and Vasileios Karakitsios reports financial support was provided by IKYDA-DAAD. Evangelia Besiou reports financial support was provided by COST Action CA15103. Iuliana Vasiliev reports financial support was provided by German Research Foundation.

Acknowledgments

We thank Ulrich Treffert for help in the organic geochemistry laboratory and Jens Fiebig for support in the Goethe University-Senckenberg BiK-F Stable Isotope Facility. This research was financed by the Greek-German collaboration project (IKYDA-DAAD): “Quantification of the environmental changes in the Eastern Mediterranean at the onset of the Messinian Salinity Crisis (Crete-Greece)” (QUANTMES) of IV and VK. Collaboration was made possible through the COST Action CA15103 “Uncovering the Mediterranean salt giant” (MEDSALT) supported by COST (European Cooperation in Science and Technology). Analyses

were supported by the DFG grant number 398614017 of IV. We thank William Ryan and the two anonymous reviewers for their comments and suggestions that significantly improved this manuscript.

Appendix A. Supplementary data

Supplementary data to this article can be found online at https://doi.org/10.1016/j.palaeo.2022.110903.

References

Antonarakou, A., Kontakiotis, G., Mortyn, P.G., Drinia, H., Sprovieri, M., Besiou, E., Tripsanas, E., 2015. Biotic and geochemical ($\delta^{18}O$, $\delta^{13}C$, Mg/Ca, Ba/ca) responses of *Globigerinoides ruber* morphotypes to upper water column variations during the last deglaciation, Gulf of Mexico. Geochim. Cosmochim. Acta 170, 69–93. https://doi.org/10.1016/j.gca.2015.08.003.

Antonarakou, A., Kontakiotis, G., Vasilatos, C., Besiou, E., Zarkogiannis, S., Drinia, H., Mortyn, P.G., Tsaparas, N., Makri, P., Karakitsios, V., 2019. Evaluating the effect of marine diagenesis on late Miocene pre-evaporitic sedimentary successions of eastern Mediterranean Sea. In: IOP Conference Series: Earth and Environmental Sciences, 221, p. 012051. https://doi.org/10.1088/1755-1315/221/1/012051.

van Assen, E., Kuiper, K.F., Barhoun, N., Krijgsman, W., Sierro, F.J., 2006. Messinian astrochronology of the Melilla Basin: stepwise restriction of the Mediterranean–Atlantic connection through Morocco. Palaeogeogr. Palaeoclimatol. Palaeoecol. 238, 15–31. https://doi.org/10.1016/j.palaeo.2006.03.014.

Bellanca, A., Caruso, A., Ferruzza, G., Neri, R., Rouchy, J.M., Sprovieri, M., Blanc-Valleron, M.M., 2001. Transition from marine to hypersaline conditions in the Messinian Tripoli Formation from the marginal areas of the central Sicilian Basin. Sediment. Geol. 140, 87–105. https://doi.org/10.1016/S0037-0738(00)00173-1.

Bemis, B.E., Spero, H.J., Bijma, J., Lea, D.W., 1998. Reevaluation of the oxygen isotopic composition of planktonic foraminifera: experimental results and revised paleotemperature equations. Paleoceanography 13 (2), 150–160. https://doi.org/10.1029/98PA00070.

Besseling, M., Hopmans, E.C., Koenen, M., van der Meer, M.T.J., Vreugdenhil, S., Schouten, S., Sinninghe Damsté, J.S., Villanueva, L., 2019. Depth-related differences in archaeal populations impact the isoprenoid tetraether lipid composition of the Mediterranean Sea water column. Org. Geochem. 135, 16–31. https://doi.org/10.1016/j.orggeochem.2019.06.008.

Bialik, O.M., Zammit, R., Micallef, A., 2021. Architecture and sequence stratigraphy of the Upper Coralline Limestone formation, Malta – implications for Eastern Mediterranean restriction prior to the Messinian Salinity Crisis. Depos. Rec. 00, 1–15. https://doi.org/10.1002/dep2.138.

Bijma, J., Faber Jr., W.W., Hemleben, Ch., 1990. Temperature and salinity limits for growth and survival of some planktonic foraminifers in laboratory cultures. J. Foraminifer. Res. 20, 95–116. https://doi.org/10.2113/gsjfr.20.2.95.

Blanc, P.L., 2006. Improved modelling of the Messinian Salinity Crisis and conceptual implications. Palaeogeogr. Palaeoclimatol. Palaeoecol. 238, 349–372. https://doi.org/10.1016/j.palaeo.2006.03.033.

Blanc-Valleron, M.-M., Pierre, C., Caulet, J.P., Caruso, A., Rouchy, J.-M., Cespuglio, G., Sprovieri, R., Pestrea, S., Di Stefano, E., 2002. Sedimentary, stable isotope and micropaleontological records of paleoceanographic change in the Messinian Tripoli Formation (Sicily, Italy). Palaeogeogr. Palaeoclimatol. Palaeoecol. 185, 255–286. https://doi.org/10.1016/S0031-0182(02)00302-4.

Bouvier-Soumagnac, Y., Duplessy, J.-C., 1985. Carbon and oxygen isotopic composition of planktonic foraminifera from laboratory culture, plankton tows and recent sediment: implications for the reconstruction of paleoclimatic conditions and of the global carbon cycle. J. Foraminiferal Res. 15, 302–320.

Brassell, S.C., Eglinton, G., Marlowe, I.T., Pflaumann, U., Sarnthein, M., 1986. Molecular stratigraphy e a new tool for climatic assessment. Nature 320, 129–133. https://doi.org/10.1038/320129a0.

Bulian, F., Sierro, F.J., Ledesma, S., Jiménez-Espejo, F.J., Bassetti, M.-A., 2021. Messinian West Alboran Sea record in the proximity of Gibraltar: early signs of Atlantic-Mediterranean gateway restriction. Mar. Geol. 434, 106430 https://doi.org/10.1016/j.margeo.2021.106430.

Bulian, F., Kouwenhoven, T.J., Jiménez-Espejo, F.J., Krijgsman, W., Andersen, N., Sierro, F.J., 2022. Impact of the Mediterranean-Atlantic connectivity and the late Miocene carbon shift on deep-sea communities in the Western Alboran Basin. Palaeogeogr. Palaeoclimatol. Palaeoecol. 589, 110841 https://doi.org/10.1016/j.palaeo.2022.110841.

Capella, W., Flecker, R., Hernández-Molina, F.J., Simon, D., Meijer, P.T., Rogerson, M., Sierro, F.J., Krijgsman, W., 2019. Mediterranean isolation preconditioning the earth system for late Miocene climate cooling. Sci. Rep. 9, 3795. https://doi.org/10.1038/s41598-019-40208-2.

Conte, M.H., Sicre, M.A., Ruhlemann, C., Weber, J.C., Schulte, S., Schulz-Bull, D., Blanz, T., 2006. Global temperature calibration of the alkenone unsaturation index (U^{K}_{37}) in surface waters and comparison with surface sediments. Geochem. Geophys. Geosyst. 7 https://doi.org/10.1029/2005gc001054.

Corbí, H., Soria, J.M., Giannetti, A., Yébenes, A., 2020. The step-by-step restriction of the Mediterranean (start, amplification, and consolidation phases) preceding the Messinian Salinity Crisis (climax phase) in the Bajo Segura basin. Geo-Mar. Lett. 40, 341–361. https://doi.org/10.1007/s00367-020-00647-7.

Cornée, J.J., Roger, S., Münch, P., Saint-Martin, J.P., Féraud, G., Conesa, G., Pestrea, S., 2002. Messinian events: new constraints from sedimentological investigations and new $^{40}Ar/^{39}Ar$ ages in the Melilla –Nador basin (Morocco). Sediment. Geol. 151, 127–147.

Di Stefano, A., Verducci, M., Lirer, F., Ferraro, L., Iaccarino, S.M., Hüsing, S.K., Hilgen, F. J., 2010. Paleoenvironmental conditions preceding the Messinian Salinity Crisis in the Central Mediterranean: Integrated data from the Upper Miocene Trave section (Italy). Palaeogeogr. Palaeoclimatol. Palaeoecol. 297 (1), 37–53. https://doi.org/10.1016/j.palaeo.2010.07.012.

Drinia, H., Antonarakou, A., Tsaparas, N., Kontakiotis, G., 2007. Palaeoenvironmental conditions preceding the Messinian salinity crisis: a case study from Gavdos Island. Geobios 40, 251–265. https://doi.org/10.1016/j.geobios.2007.02.003.

El Achalhi, M., Münch, P., Cornée, J.J., Azdimousa, A., Melinte-Dobrinescu, M., Quillévéré, F., Drinia, H., Fauquette, S., Jiménez-Moreno, G., Merzeraud, G., Ben, Moussa A., El Kharim, Y., Feddi, N., 2016. The late Miocene Mediterranean-Atlantic connections through the North Rifian Corridor: New insights from the Boudinar and Arbaa Taourirt basins (northeastern Rif, Morocco). Palaeogeogr. Palaeoclimatol. Palaeoecol. 459, 131–152.

Elderfield, H., Vautravers, M., Cooper, M., 2002. The relationship between shell size and Mg/Ca, Sr/Ca, $\delta^{18}O$, and $\delta^{13}C$ of species of planktonic foraminifera. Geochem. Geophys. Geosyst. 3 (8), 4052. https://doi.org/10.1029/2001GC000194.

Elling, F.J., Gottschalk, J., Doeana, K.D., Kusch, S., Hurley, S.J., Pearson, A., 2019. Archaeal lipid biomarker constraints on the Paleocene-Eocene carbon isotope excursion. Nat. Commun. 10 (1) https://doi.org/10.1038/s41467-019-12553-3.

Emeis, K.C., Struck, U., Schulz, H.M., Rosenberg, R., Bernasconi, S., Erlenkeuser, H., Sakamoto, T., Martinez-Ruiz, F., 2000. Temperature and salinity variations of Mediterranean Sea surface waters over the last 16,000 years from records of planktonic stable oxygen isotopes and alkenone unsaturation ratios. Palaeogeogr. Palaeoclimatol. Palaeoecol. 158, 259–280. https://doi.org/10.1016/S0031-0182(00)00053-5.

Fenton, M., Geiselhart, S., Rohling, E.J., Hemleben, Ch., 2000. Aplanktonic zones in the Red Sea. Mar. Micropaleontol. 40, 277–294. https://doi.org/10.1016/S0377-8398(00)00042-6.

Flecker, R., Krijgsman, W., Capella, W., de Castro Martíns, C., Dmitrieva, E., Mayser, J.P., Marzocchi, A., Modestu, S., Ochoa, D., Simon, D., Tulbure, M., van den Berg, B., van der Schee, M., de Lange, G., Ellam, R., Govers, R., Gutjahr, M., Hilgen, F., Kouwenhoven, T., Lofi, J., Meijer, P., Sierro, F.J., Bachiri, N., Barhoun, N., Alami, A. C., Chacon, B., Flores, J.A., Gregory, J., Howard, J., Lunt, D., Ochoa, M., Pancost, R., Vincent, S., Yousfi, M.Z., 2015. Evolution of the Late Miocene Mediterranean–Atlantic gateways and their impact on regional and global environmental change. Earth Sci. Rev. 150, 365–392. https://doi.org/10.1016/j.earscirev.2015.08.007.

Gennari, R., Lozar, F., Turco, E., Dela, Pierre F., Manzi, V., Natalicchio, M., Lugli, S., Roveri, M., Schreiber, C., Taviani, M., 2018. Integrated stratigraphy and paleoceanographic evolution of the pre-evaporitic phase of the Messinian salinity crisis in the Eastern Mediterranean as recorded in the Tokhni section (Cyprus island). Newsl. Stratigr. 51, 1–23. https://doi.org/10.1127/nos/2017/0350.

Gladstone, R., Flecker, R., Valdes, P., Lunt, D., Markwick, P., 2007. The Mediterranean hydrologic budget from a late Miocene global climate simulation. Palaeogeogr. Palaeoclimatol. Palaeoecol. 251, 254–267. https://doi.org/10.1016/j.palaeo.2007.03.050.

Herbert, T.D., Lawrence, K.T., Tzanova, A., Peterson, L.C., Caballero-Gill, R., Kelly, C.S., 2016. Late Miocene global cooling and the rise of modern ecosystems. Nat. Geosci. 9, 843–847. https://doi.org/10.1038/NGEO2813.

Hilgen, F.J., Krijgsman, W., 1999. Cyclostratigraphy and astrochronology of the Tripoli diatomite Formation (pre-evaporite Messinian, Sicily, Italy). Terra Nova 11, 16–22. https://doi.org/10.1046/j.1365-3121.1999.00221.x.

Hilgen, F.J., Krijgsman, W., Langereis, C.G., Lourens, L.J., Santarelli, A., Zachariasse, W. J., 1995. Extending the astronomical (polarity) time scale into the Miocene. Earth Planet. Sci. Lett. 136, 495–510. https://doi.org/10.1016/0012-821X(95)00207-S.

Hilgen, F., Krijgsman, W., Wijbrans, J.R., 1997. Direct comparison of astronomical and $^{40}Ar/^{39}Ar$ ages of ash beds: potential implications for the age of mineral dating standards. Geophys. Res. Lett. 24 (16), 2043–2046. https://doi.org/10.1029/97GL02029.

Hilgen, F.J., Bissoli, L., Iaccarino, S., Krijgsman, W., Meijer, R., Negri, A., Villa, G., 2000. Integrated stratigraphy and astrochronology of the Messinian GSSP at Oued Akrech (Atlantic Morocco). Earth Planet. Sci. Lett. 182, 237–251. https://doi.org/10.1016/S0012-821X(00)00247-8.

van Hinsbergen, D.J.J., Meulenkamp, J.E., 2006. Neogene supradetachment basin development on Crete (Greece) during exhumation of the South Aegean core complex. Basin Res. 18, 103–124. https://doi.org/10.1111/j.1365-2117.2005.00282.x.

Hodell, D.A., Benson, R.H., Kent, D.V., Boersma, A., Rakic-El Bied, K., 1994. Magnetostratigraphic, biostratigraphic, and stable isotope stratigraphy of an Upper Miocene drill core from the Salé Briqueterie (Northwest Morocco): A high-resolution chronology for the Messinian stage. Paleoceanography 9 (6), 835–855. https://doi.org/10.1029/94PA01838.

Hsü, K.J., 1972. Origin of saline giants: a critical review after the discovery of the Mediterranean evaporites. Earth Sci. Rev. 8, 371–396. https://doi.org/10.1016/0012-8252(72)90062-1.

Hsü, K.J., Ryan, W.B.F., Cita, M.B., 1973. Late Miocene desiccation of the Mediterranean. Nature 242, 240–244.

Hüsing, S.K., Kuiper, K.F., Link, W., Hilgen, F.J., Krijgsman, W., 2009. The upper Tortonian–lower Messinian at Monte Dei Corvi (Northern Apennines, Italy): Completing a Mediterranean reference section for the Tortonian Stage. Earth Planet. Sci. Lett. 282 (1–4), 140–157. https://doi.org/10.1016/j.epsl.2009.03.010.

Ilyina, L.B., Shcherba, I.G., Khondkarian, S., 2004. Map 8: Middle late Miocene (late Tortonian – early Messinian – early Maeotian – late Pannonian) in *Lithological-*

Paleogeographic maps of Paratethys. In: Popov, S.V., Rögl, F., Rozanov, A.Y., Steininger, F.F., Shcherba, I.G., Kovac, M. (Eds.), Courier Forschungsinstitut Senckenberg, vol. 250 maps 1-10 (annex), Late Eocene to Pliocene.

Ivanovic, R.F., Valdes, P.J., Flecker, R., Gutjahr, M., 2014. Modelling global-scale climate impacts of the late Miocene Messinian Salinity Crisis. Clim. Past 10, 607–622. https://doi.org/10.5194/cp-10-607-2014.

Kallel, N., Paterne, M., Duplessy, J.C., Vergnaud-Grazzini, C., Pujol, C., Labeyrie, L.D., Arnold, M., Fontugne, M., Pierre, C., 1997. Enhanced rainfall on Mediterranean region during the last sapropel event. Oceanol. Acta 20 (5), 697–712.

Karakitsios, V., Roveri, M., Lugli, S., Manzi, V., Gennari, R., Antonarakou, A., Triantaphyllou, M., Agiadi, K., Kontakiotis, G., Kafousia, N., de Rafelis, M., 2017a. A record of the Messinian salinity crisis in the eastern Ionian tectonically active domain (Greece, eastern Mediterranean). Basin Res. 29 (2), 203–233. https://doi.org/10.1111/bre.12173.

Karakitsios, V., Cornée, J.-J., Tsourou, T., Moissette, P., Kontakiotis, G., Agiadi, K., Manoutsoglou, E., Triantaphyllou, M., Koskeridou, E., Drinia, H., Roussos, D., 2017b. Messinian salinity crisis record under strong freshwater input in marginal, intermediate, and deep environments: the case of the North Aegean. Palaeogeogr. Palaeoclimatol. Palaeoecol. 485, 316–335. https://doi.org/10.1016/j.palaeo.2017.06.023.

Karami, M.P., de Leeuw, A., Krijgsman, W., Meijer, P.Th., Wortel, M.J.R., 2011. The role of gateways in the evolution of temperature and salinity of semi-enclosed basins: an oceanic box model for the Miocene Mediterranean Sea and Paratethys. Glob. Planet. Chang. 79, 73–88. https://doi.org/10.1016/j.gloplacha.2011.07.011.

Kim, J.-H., Schouten, S., Hopmans, E.C., Donner, B., Sinninghe Damsté, J.S., 2008. Global sediment core-top calibration of the TEX_{86} paleothermometer in the ocean. Geochim. Cosmochim. Acta 72 (4), 1154–1173. https://doi.org/10.1016/i.gca.2007.12.010.

Kim, J.-H., van der Meer, J., Schouten, S., Helmke, P., Willmott, V., Sangiorgi, F., Koç, N., Hopmans, E., Sinninghe Damsté, J.S., 2010. New indices and calibrations derived from the distribution of crenarchaeal isoprenoid tetraether lipids: Implications for past sea surface temperature reconstructions. Geochim. Cosmochim. Acta 74 (16). https://doi.org/10.1016/j.gca.2010.05.027.

Kim, J.-H., Schouten, S., Rodrigo-Gámiz, M., Rampen, S., Marino, G., Huguet, C., Helmke, P., Buscail, R., Hopmans, E.C., Pross, J., Sangiorgi, F., Middelburg, J.B.M., Sinninghe Damsté, J.S., 2015. Influence of deep-water derived isoprenoid tetraether lipids on the TEX_{86}^{H} paleothermometer in the Mediterranean Sea. Geochim. Cosmochim. Acta 150, 125–141. https://doi.org/10.1016/j.gca.2014.11.017.

Kontakiotis, G., Karakitsios, V., Mortyn, P.G., Antonarakou, A., Drinia, H., Anastasakis, G., Agiadi, K., Kafousia, N., De Rafelis, M., 2016. New insights into the early Pliocene hydrographic dynamics and their relationship to the climatic evolution of the Mediterranean Sea. Palaeogeogr. Palaeoclimatol. Palaeoecol. 459, 348–364. https://doi.org/10.1016/j.palaeo.2016.07.025.

Kontakiotis, G., Besiou, E., Antonarakou, A., Zarkogiannis, S.D., Kostis, A., Mortyn, P.G., Moissette, P., Cornée, J.-J., Schulbert, C., Drinia, H., Anastasakis, G., Karakitsios, V., 2019. Decoding Sea surface and paleoclimate conditions in the eastern Mediterranean over the Tortonian-Messinian transition. Palaeogeogr. Palaeoclimatol. Palaeoecol. 534, 109312 https://doi.org/10.1016/j.palaeo.2019.109312.

Kouwenhoven, T.J., Seidenkrantz, M.S., Van Der Zwaan, G.J., 1999. Deep-water changes: the near-synchronous disappearance of a group of benthic foraminifera from the late Miocene Mediterranean. Palaeogeogr. Palaeoclimatol. Palaeoecol. 152, 259–281. https://doi.org/10.1016/S0031-0182(99)00065-6.

Kouwenhoven, T.J., Hilgen, F.J., Van der Zwaan, G.J., 2003. Late Tortonian–early Messinian stepwise disruption of the Mediterranean–Atlantic connections: constraints from benthic foraminiferal and geochemical data. Palaeogeogr. Palaeoclimatol. Palaeoecol. 198, 303–319. https://doi.org/10.1016/S0031-0182(03)00472-3.

Kouwenhoven, T.J., Morigi, C., Negri, A., Giunta, S., Krijgsman, W., Rouchy, J.M., 2006. Paleoenvironmental evolution of the eastern Mediterranean during the Messinian: Constraints from integrated microfossil data of the Pissouri Basin (Cyprus). Mar. Micropaleontol. 60, 17–44. https://doi.org/10.1016/j.marmicro.2006.02.005.

Krijgsman, W., Hilgen, F.J., Raffi, I., Sierro, F.J., Wilson, D.S., 1999a. Chronology, causes and progression of the Messinian salinity crisis. Nature 400, 652–655. https://doi.org/10.1038/23231.

Krijgsman, W., Langereis, C.G., Zachariasse, W.J., Boccaletti, M., Moratti, G., Gelati, R., Iaccarino, S., Papani, G., Villa, G., 1999b. Late Neogene evolution of the Taza-Guercif Basin (Rifian Corridor, Morocco) and implications for the Messinian salinity crisis. Mar. Geol. 153, 147–160. https://doi.org/10.1016/S0025-3227(98)00084-X.

Krijgsman, W., Capella, W., Simon, D., Hilgen, F.J., Kouwenhoven, T.J., Meijer, P.Th., Sierro, F.J., Tulbure, M.A., van den Berg, B.C.J., van der Schee, M., Flecker, R., 2018. The Gibraltar Corridor: Watergate of the Messinian Salinity Crisis. Mar. Geol. 403, 238–246. https://doi.org/10.1016/j.margeo.2018.06.008.

Kuiper, K.F., Hilgen, F., Steenbrink, J., Wijbrans, J.R., 2004. $^{40}Ar/^{39}Ar$ ages of tephras intercalated in astronomically tuned Neogene sedimentary sequences in the Eastern Mediterranean. Earth Planet. Sci. Lett. 222 (2), 583–597. https://doi.org/10.1016/j.epsl.2004.03.005.

Laskar, J., Robutel, P., Joutel, F., Gastineau, M., Correia, A.C.M., Levrard, B., 2004. A long-term numerical solution for the insolation quantities of the Earth. Astron. Astrophys. 428, 261–285. https://doi.org/10.1051/0004-6361:20041335.

Laube-Lenfant, E., 1996. Utilisation des isotopes naturels ^{18}O de l'eau et ^{13}C du carbone inorganique dissous comme traceurs océaniques dans les zones frontales et d'upwelling. Cas du Pacifique équatorial et de la mer d'Alboran. Doctoral Thesis. University Pierre et Marie Curie, 319 pp.

LeGrande, A.N., Schmidt, G.A., 2006. Global gridded data set of the oxygen isotopic composition in seawater. Geophys. Res. Lett. 33 (12), L12604. https://doi.org/10.1029/2006GL026011.

Leider, A., Hinrichs, K., Mollenhauer, G., Versteegh, G., 2010. Core-top calibration of the lipid-based $U_{37}^{K'}$ and TEX_{86} temperature proxies on the southern Italian shelf (SW Adriatic Sea, Gulf of Taranto). Earth Planet. Sci. Lett. 300, 112–124.

Lourens, L.J., Hilgen, F.J., Laskar, J., Shackleton, N.J., Wilson, D.S., 2004. The Neogene Period. In: Gradstein, F.M., Ogg, J.G., Smith, A.G. (Eds.), A Geologic Time Scale 2004. Cambridge University Press, Cambridge, pp. 409–440. https://doi.org/10.1017/CBO9780511536045.

Madof, A.S., Bertoni, C., Lofi, J., 2019. Discovery of vast fluvial deposits provides evidence for drawdown during the late Miocene Messinian salinity crisis. Geology 47, 171–174. https://doi.org/10.1130/G45873.1.

Manzi, V., Gennari, R., Hilgen, F., Krijgsman, W., Lugli, S., Roveri, M., Sierro, F.J., 2013. Age refinement of the Messinian salinity crisis onset in the Mediterranean. Terra Nova 25, 315–322. https://doi.org/10.1111/ter.12038.

Mayser, J.P., Flecker, R., Marzzochi, A., Kouwvernhoven, T.J., Lunt, D.J., Pancost, R.D., 2017. Precession driven changes in terrestrial organic matter input to the Eastern Mediterranean leading up to the Messinian Salinity Crisis. Earth Planet. Sci. Lett. 462, 199–211. https://doi.org/10.1016/j.epsl.2017.01.029.

Mehta, S., Singh, A., Thirumalai, K., 2021. Uncertainty in paleosalinity estimates from foraminiferal geochemical records in the northern Indian Ocean. Palaeogeogr. Palaeoclimatol. Palaeoecol. 569, 110326 https://doi.org/10.1016/j.palaeo.2021.110326.

Meijer, P.T., 2012. Hydraulic theory of sea straits applied to the onset of the Messinian Salinity Crisis. Mar. Geol. 326, 131–139. https://doi.org/10.1016/j.margeo.2012.09.001.

Miller, K.G., Mountain, G.S., Wright, J.D., Browning, J.V., 2011. A 180-million-year record of sea level and ice volume variations from continental margin and deep-sea isotopic records. Oceanography 24 (2), 40–53. https://doi.org/10.5670/oceanog.2011.26.

Moissette, P., Cornée, J.-J., Antonarakou, A., Kontakiotis, G., Drinia, H., Koskeridou, E., Tsourou, T., Agiadi, K., Karakitsios, V., 2018. Palaeoenvironmental changes at the Tortonian/Messinian boundary: A deep-sea sedimentary record of the eastern Mediterranean Sea. Palaeogeogr. Palaeoclimatol. Palaeoecol. 505, 217–233. https://doi.org/10.1016/j.palaeo.2018.05.046.

Müller, P.J., Kirst, G., Ruhland, G., von Storch, I., Rosell-Melé, A., 1998. Calibration of the alkenone paleotemperature index $U_{37}^{K'}$ based on core-tops from the eastern South Atlantic and the global ocean (60°N–60°S). Geochim. Cosmochim. Acta 62, 1757–1772. https://doi.org/10.1016/S0016-7037(98)00097-0.

Pellegrino, L., Dela Pierre, F., Natalicchio, M., Carnevale, G., 2018. The Messinian diatomite deposition in the Mediterranean region and its relationships to the global silica cycle. Earth Sci. Rev. 178, 154–176. https://doi.org/10.1016/j.earscirev.2018.01.018.

Pierre, C., 1999. The oxygen and carbon isotope distribution in the Mediterranean water masses. Mar. Geol. 153, 41–55. https://doi.org/10.1016/S0025-3227(98)00090-5.

Prahl, F.G., Wakeham, S.G., 1987. Calibration of unsaturation patterns in long-chain ketone compositions for paleotemperature assessment. Nature 330 (6146), 367–369. https://doi.org/10.1038/330367a0.

Robertson, A.H.F., Parlak, O., Ustaömer, T., 2012. Overview of the Palaeozoic–Neogene evolution of Neotethys in the Eastern Mediterranean region (Southern Turkey, Cyprus, Syria). Pet. Geosci. 18, 381–404. https://doi.org/10.1144/petgeo2011-091.

Roger, S., Münch, P., Cornée, J.J., Saint-Martin, J.P., Fraud, G., Conesa, G., Pestrea, S., Ben Moussa, A., 2000. $^{40}Ar/^{39}Ar$ dating of the preevaporitic Messinian marine sequences of the Melilla basin (Morocco): a proposal for some bio-sedimentary events as isochrons around the Alboran Sea. Earth Planet. Sci. Lett. 179, 101–113.

Rohling, E.J., Marino, G., Grant, K.M., 2015. Mediterranean climate and oceanography, and the periodic development of anoxic events (sapropels). Earth Sci. Rev. 143, 62–97. https://doi.org/10.1016/j.earscirev.2015.01.008.

Roveri, M., Flecker, R., Krijgsman, W., Lofi, J., Lugli, S., Manzi, V., Sierro, F.J., Bertini, A., Camerlenghi, A., De Lange, G., Govers, R., Hilgen, F.J., Hübscher, C., Meijer, P.T., Stoica, M., 2014. The Messinian Salinity Crisis: past and future of a great challenge for marine sciences. Mar. Geol. 352, 25–58. https://doi.org/10.1016/j.margeo.2014.02.002.

Sabino, M., Schefuß, E., Natalicchio, M., Dela Pierre, F., Birgel, D., Bortels, D., Schnetger, B., Peckmann, J., 2020. Climatic and hydrologic variability in the northern Mediterranean across the onset of the Messinian salinity crisis. Palaeogeogr. Palaeoclimatol. Palaeoecol. 545, 109632 https://doi.org/10.1016/j.palaeo.2020.109632.

Sabino, M., Birgel, D., Natalicchio, M., Dela Pierre, F., Peckmann, J., 2021. Carbon isotope excursions during the late Miocene recorded by lipids of marine Thaumarchaeota, Piedmont Basin, Mediterranean Sea. Geology 50 (1), 32–36. https://doi.org/10.1130/G49360.1.

Santarelli, A., Brinkhuis, H., Hilgen, F.J., Lourens, L.J., Versteegh, G.J.M., Visscher, H., 1998. Orbital signatures in a late Miocene dinoflagellate record from Crete (Greece). Mar. Micropaleontol. 33, 273–297. https://doi.org/10.1016/S0377-8398(97)00042-X.

Schouten, S., Hopmans, E.C., Schefuss, E., Sinninghe Damsté, J.S., 2002. Distributional variations in marine crenarchaeotal membrane lipids: a new tool for reconstructing ancient sea water temperatures? Earth Planet. Sci. Lett. 204 (1–2), 265–274. https://doi.org/10.1016/s0012-821x(02)00979-2.

Schouten, S., Hopmans, E.C., Sinninghe Damsté, J.S., 2013. The organic geochemistry of glycerol dialkyl glycerol tetraether lipids: A review. Org. Geochem. 54, 19–61. https://doi.org/10.1016/j.orggeochem.2012.09.006.

Schuster, M., Duringer, P., Ghienne, J.F., Vignaud, P., Mackaye, H.T., Likius, A., Brunet, M., 2006. The age of the Sahara Desert. Science 311, 821. https://doi.org/10.1126/science.1120161.

Seidenkrantz, M.-S., Kouwenhoven, T.J., Jorissen, F.J., Shackleton, N.J., van der Zwaan, G.J., 2000. Benthic foraminifera as indicators of changing Mediterranean–Atlantic water exchange in the late Miocene. Mar. Geol. 163, 387–407. https://doi.org/10.1016/S0025-3227(99)00116-4.

Siddall, M., Rohling, E.J., Almogi-Labin, A., Hemleben, Ch., Meischner, D., Schmelzer, I., Smeed, D.A., 2003. Sea-level fluctuations during the last glacial cycle. Nature 423 (6942), 853–858. https://doi.org/10.1038/nature01690.

Sierro, F.J., Hilgen, F.J., Krijgsman, W., Flores, J.A., 2001. The Abad composite (SE Spain): a Messinian reference section for the Mediterranean and the APTS. Palaeogeogr. Palaeoclimatol. Palaeoecol. 168, 141–169. https://doi.org/10.1016/S0031-0182(00)00253-4.

Sierro, F.J., Flores, J.A., Frances, G., Vazquez, A., Utrilla, R., Zamarreno, I., Erlenkeuser, H., Barcena, M.A., 2003. Orbitally-controlled oscillations in planktic communities and cyclic changes in western Mediterranean hydrography during the Messinian. Palaeogeogr. Palaeoclimatol. Palaeoecol. 190, 289–316. https://doi.org/10.1016/S0031-0182(02)00611-9.

Simon, D., Meijer, P., 2015. Dimensions of the Atlantic–Mediterranean connection that caused the Messinian Salinity Crisis. Mar. Geol. 364, 53–64. https://doi.org/10.1016/j.margeo.2015.02.004.

Simon, D., Marzocchi, A., Flecker, R., Lunt, D., Hilgen, F., Meijer, P., 2017. Quantifying the Mediterranean freshwater budget throughout the late salinity crisis. Earth Planet. Sci. Lett. 472, 25–37. https://doi.org/10.1016/j.epsl.2017.05.013.

Tzanova, A., Herbert, T.D., Peterson, L., 2015. Cooling Mediterranean Sea surface temperatures during the late Miocene provide a climate context for evolutionary transitions in Africa and Eurasia. Earth Planet. Sci. Lett. 419, 71–80. https://doi.org/10.1016/j.epsl.2015.03.016.

Uno, K.T., Polissar, P.J., Jackson, K.E., deMenocal, P.B., 2016. Neogene biomarker record of vegetation change in eastern Africa. Proc. Natl. Acad. Sci. 113 (23), 6355–6363. https://doi.org/10.1073/pnas.1521267113.

Vasiliev, I., Mezger, E.M., Lugli, S., Reichart, G.J., Manzi, V., Roveri, M., 2017. How dry was the Mediterranean during the Messinian Salinity Crisis? Palaeogeogr. Palaeoclimatol. Palaeoecol. 471, 120–133. https://doi.org/10.1016/j.palaeo.2017.01.032.

Vasiliev, I., Karakitsios, V., Bouloubassi, I., Agiadi, K., Kontakiotis, G., Antonarakou, A., Triantaphyllou, M., Gogou, A., Kafousia, N., de Rafélis, M., Zarkogiannis, S., Kaczmar, F., Parinos, C., Pasadakis, N., 2019. Large sea surface temperature, salinity, and productivity-preservation changes preceding the onset of the Messinian Salinity Crisis in the eastern Mediterranean Sea. Paleoceanogr. Paleoclimatol. 34 (2), 182–202. https://doi.org/10.1029/2018PA003438.

Volkman, J.K., Barrett, S.M., Blackburn, S.I., Sikes, E.L., 1995. Alkenones in *Gephyrocapsa oceanica*: implications for studies of paleoclimate. Geochim. Cosmochim. Acta 59 (3), 513–520. https://doi.org/10.1016/0016-7037(95)00325-t.

Williams, D.F., Bé, A.W.H., Fairbanks, R.G., 1981. Seasonal stable isotopic variations in living planktonic foraminifera from Bermuda plankton tows. Palaeogeogr. Palaeoclimatol. Palaeoecol. 33, 71–102.

Williams, M., Haywood, A.M., Taylor, S.P., Valdes, P.J., Sellwood, B.W., Hillenbrand, C. D., 2005. Evaluating the efficacy of planktonic foraminifer calcite delta O-18 data for sea surface temperature reconstruction for the late Miocene. Geobios 38, 843–863. https://doi.org/10.1016/j.geobios.2004.12.001.

Zachariasse, W.J., Lourens, L.J., 2021. The Messinian on Gavdos (Greece) and the status of currently used ages for the onset of the MSC and gypsum precipitation. Newsl. Stratigr. https://doi.org/10.1127/nos/2021/0677.

Zachariasse, W.J., van Hinsbergen, D.J.J., Fortuin, A.R., 2011. Formation and fragmentation of a late Miocene supradetachment basin in Central Crete: implications for exhumation mechanisms of high-pressure rocks in the Aegean forearc. Basin Res. 23, 678–701. https://doi.org/10.1111/j.1365-2117.2011.00507.x.

Zachariasse, W.J., Kontakiotis, G., Lourens, L.J., Antonarakou, A., 2021. The Messinian of Agios Myron (Crete, Greece): A key to better understanding diatomite formation south of Crete, on Gavdos Island. Palaeogeogr. Palaeoclimatol. Palaeoecol. 581, 110633 https://doi.org/10.1016/j.palaeo.2021.110633.